

Thesis

Numerical Modeling of CIGS Solar Cells:

Definition of the Baseline and

Explanation of Superposition Failure

Submitted by

Markus Gloeckler

Department of Physics

In partial fulfillment of the requirements

for the Degree of Master of Science

Colorado State University

Fort Collins, Colorado

Spring 2003

Colorado State University

December 05, 2002

We hereby recommend that the thesis prepared under our supervision by Markus Gloeckler entitled "Numerical Modeling of CIGS Solar Cells: Definition of the Baseline and Explanation of Superposition Failure" be accepted as fulfilling in part requirements for the degree of Master of Science.

Graduate Committee

Advisor

Department Head

Abstract

Numerical Modeling of CIGS Solar Cells: Definition of the Baseline and Explanation of Superposition Failure

Abstract: Numerical modeling tools have become increasingly useful with the amount of processing power that is available today. A three-layer structure, simulating a Cu(InGa)Se₂ (CIGS) heterojunction solar cell, was set up using the AMPS software. Special care was taken in the selection of input parameters; values are chosen based on experimental data, literature values, theory, and reasonable estimates. Comprehensive studies were performed to investigate the sensitivity of solar-cell performance to each input parameter.

It was possible to model an experimental CIGS device that showed non-superposition between light and dark current voltage data. The dark curves were shifted to significantly higher voltages. This effect is explained by a photo-modulated barrier that results from a reasonable conduction band offsets at the CdS/CIGS interface and a high density of defect states in the CdS layer. This work also investigates why this effect becomes more significant at low temperatures and how it varies with light intensity and wavelength.

Markus Gloeckler
Department of Physics
Colorado State University
Fort Collins, CO 80523
Spring 2003

Acknowledgements

First of all, I want to thank all the members of the Photovoltaic Laboratory at CSU. Special thanks go to my advisor Jim Sites for direction and lead, but also for giving me the freedom to work independently. Thanks for the help and the hours of fruitful discussions to Alex Pudov and Pam Johnson.

This work was made feasible through the Institute of Energy Conversion at the University of Delaware that provided the solar cell samples studied and relevant information. Thanks to Caroline Jenkins, who did most of the initial experimental characterization of the studied samples.

This work used the computer code AMPS provided by the Pennsylvania State University, where it was developed with support from the Electric Power Research Institute.

This work was supported by the U.S. National Renewable Energy Laboratory.

Table of Contents

Chapter 1 Introduction.....	1
Chapter 2 Background	3
2.1 Device Structure of CIGS Solar Cells.....	3
2.2 Output Parameters of Interest in Photovoltaic Operation	4
2.3 Band Offsets	8
Chapter 3 AMPS Modeling – Base Case	12
3.1 Description of the Base Case	12
3.2 General Device Properties.....	15
3.3 Layer Properties	16
3.4 Defect States.....	18
3.5 Modeling Results for the Base Case	22
Chapter 4 AMPS Modeling-Variational Cases.....	24
4.1 Parameter Variations vs. Modeling Output (JV and QE).....	24
4.2 CdS.....	26
4.3 CIGS – Basic Properties.....	26
4.4 CIGS - Defect States	27
4.5 CIGS – Tail States.....	30
4.6 Band Offsets – Electron Affinities.....	31
4.7 Temperature	33
Chapter 5 Modeling of an Experimental Device	35
5.1 Description of the IEC Device	35
5.2 Modeling: Best Fit for the IEC Device	37
5.3 Band Diagram of the Best Fit.....	40
5.4 Modeling: Variations on the Best Fit	42
5.5 Variation in Illumination Intensity.....	45
5.6 Single Wavelength Illumination and the “red kink”	48
5.7 Limitations of the Model.....	52
Chapter 6 Conclusions	53

List of Figures

Figure 1: CIGS structure.....	4
Figure 2: J-V Characteristics with important parameters	5
Figure 3: J-V data on a logarithmic scale	6
Figure 4: Measured and calculated quantum efficiency	7
Figure 5: ZnO/CdS/CIGS structure separated. Conduction and valence-band edges shown by solid lines. Zero defined by ZnO conduction band edge.....	8
Figure 6: Band diagram for ZnO/CdS/CIGS structure	9
Figure 7: AM1.5 illumination spectrum	14
Figure 8: Absorption spectra for ZnO, CdS, and CIGS	18
Figure 9: Allowed transitions in the Shockley-Read-Hall model.....	19
Figure 10: Base case results.....	23
Figure 11: Impact on cell performance with variations in CIGS defect density	29
Figure 12: Variations in J-V due to electron affinity of the CdS.....	31
Figure 13: Variations in J-V due to the electron affinity of CIGS.....	32
Figure 14: Experimental J-V-T data	36
Figure 15: Best fit with experimental J-V-T data at 238 K, 268 K, 298 K.....	38
Figure 16: Best fit with experimental QE.....	39
Figure 17: Best fit – conduction band diagram at T = 298 K	40
Figure 18: Best fit – conduction band diagram at T = 238 K	41
Figure 19: V-T - variation in band offsets (electron affinities)	42
Figure 20: V-T - barrier shift (changing both offsets).....	43

Figure 21: V-T - variations in carrier density in CdS and CIGS	43
Figure 22: V-T - variations in defect density in CdS and CIGS	43
Figure 23: V-T - variations in capture cross-sections in CdS and CIGS	44
Figure 24: Modeled J-V for 100%, 10%, 1%, and 0% illumination.....	46
Figure 25: Experimental J-V for 100%, 11.5%, 3.5%, and 0% illumination.....	47
Figure 26: Band structure with varying illumination.....	47
Figure 27: Barrier height and “ V_{oc} ” equivalent versus intensity	48
Figure 28: Calculated J-V with single wavelength illumination.....	49
Figure 29: J-V at dark, red, and AM1.5 illumination (experimental).....	50
Figure 30: Red kink (modeling results)	51

List of Tables

Table 1: Parameters for the base case	13
Table 2: Defect densities.....	20
Table 3: Magnitude of changes	24
Table 4: Variations on the base case	25
Table 5: Barrier shifts variations	31
Table 6: Temperature dependent parameters and their values for $T = 238\text{K} - 328\text{K}$	33
Table 7: Changes from the base case	37
Table 8: Best fit and experimental device in comparison.....	38

Chapter 1

Introduction

Global warming is projected to raise the average temperature of the earth's atmosphere by 1.4 – 5.8 °C by the end of this century [1]. Finding access to a clean form of energy, with little or no emissions and environmental friendly technology, will be one of the major challenges of the 21st century. One promising attempt is the application of solar cells to utilize the immense amounts of energy that the earth receives with every second from the sun. While several techniques are employed today to achieve higher efficiency, the most likely to succeed are thin-film solar cells. Produced by inexpensive deposition techniques on inexpensive substrates, they have the potential to become an economically competitive energy source within the next decade. Solar cells based on $\text{CuIn}_{1-x}\text{Ga}_x\text{Se}_2$ (CIGS) have achieved the highest efficiency of all thin film solar cells. Maximum conversion efficiencies for laboratory-sized samples with $x \approx 0.2$ have been reported as high as 18.8 % [2].

While various methods are used today to investigate and improve CIGS devices, many questions remain unanswered. Numerical modeling helps us understand certain device properties and processes that take place in solar cell operation. A model, which is based on reasonable assumptions, and applies the known theory of solar cells, as far as we understand it today, can substantially help in the analysis. The work presented here used the AMPS software developed at the Pennsylvania State University by S. Fonash et al. Its development was supported by the Electric Power Research Institute. The term

AMPS abbreviates "Analysis of Microelectronic and Photonic Structures" and represents a computer code which allows the analysis of a broad variety of device structures under illumination or voltage bias or both. A detailed description of the solution techniques can be found in the AMPS manual [3]. Using as much experimental data as is available, modeling represents a meet-in-the-middle process where theory and experiments come together and find agreement in the calculated and experimental output. In the agreement lies the gain in knowledge, transferring the information that was used for the modeling to the experimental device. Nonetheless, modeling can be misleading because of its complexity, and near-identical results for a limited data set can often be found using different assumptions. Therefore, every result must be carefully checked, preferably through a thorough set of experimental data.

A commonly observed feature in CIGS solar cells is the lack of superposition between light and dark current-voltage data. While the basic theory of solar cells predicts the current shift I_L should be a constant for all voltages, CIGS solar cells often show deviations from this ideal behavior. Recently measured samples were found to show non-superposition in the form of a shift to higher voltages of the dark current-voltage curves. The shift increased at lower temperatures creating an excessive voltage progression $\Delta V/\Delta T$ of about -3.3 mV/K. Using the modeling technique, it will be shown that this effect can be explained assuming conduction band offsets at the ZnO-CdS and CdS-CIGS interfaces. Good agreement with the experimental data has been produced. Furthermore, increasing the offsets slightly beyond what is needed to model the current experimental devices causes a major reduction in fill factor, which has historically been labeled as the "red kink" effect.

Chapter 2

Background

After discussing the basic device structure of CIGS solar cells, the commonly used output parameters are introduced. These parameters are derived either from experimental measurements or from the output of the modeling software. In the last section of this chapter, band offsets are defined and discussed.

2.1 Device Structure of CIGS Solar Cells

Solar cells based on p-type CIGS absorbers have been fabricated on glass, mylar or stainless steel substrates using various deposition techniques. A typical structure is shown in Figure 1. Incident light is partially blocked by the metallic grid, which covers approximately 5% of the semiconductor device, and partially reflected by the surface of the transparent-conducting-oxide (TCO) layer, due to the difference in the index of refraction. Some short-wavelength photons are absorbed in the n-CdS layer. Most of the light, however, enters the semiconductor and is absorbed in the CIGS. Thicknesses, as they were used for the modeling (see Chapter 3), are given in parenthesis; only the gray shaded layers are defined explicitly within the AMPS model.

The metal contacts (Al and Mo) are only characterized by their work function, since other properties are not critical to the photovoltaic operation. The ZnO and CdS layers are usually n-type, and the CIGS p-type. The junction is formed at or near the CdS-CIGS (n-p) interface. Electrons that are generated within the junction-field region

or within one diffusion length of the junction will be collected. Chapter 4 will discuss how the recombination current affects the device output characteristics.

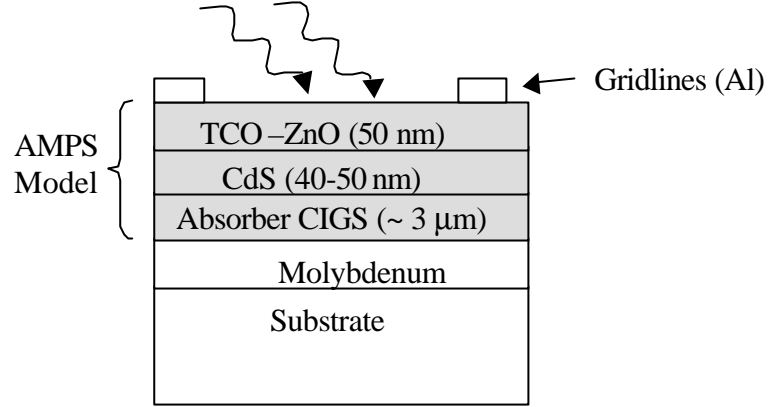


Figure 1: CIGS structure

2.2 Output Parameters of Interest in Photovoltaic Operation

The light current-voltage (I-V) characteristics of a good quality solar cell can be reasonably described by the diode equation with an additional constant term given by the light generated current:

$$I = I_0 \left(e^{qV / AkT} - 1 \right) - I_L, \quad (2.1)$$

where I_0 is the reverse bias saturation current and I_L the light generated current. “A” is the diode quality factor (ideal diode $A = 1$), which is determined by the recombination current that takes place during the photovoltaic operation. Non-ideal solar cells will also have losses due to a non-negligible series resistance R_s and a finite shunt resistance R_{sh} . Incorporating these losses, the above equation becomes:

$$I = I_0 \left(e^{q(V - IR_s) / AkT} - 1 \right) + (V - IR_s) / R_{sh} - I_L \quad (2.2)$$

AMPS generated output does not directly include the effect of series or shunt resistance, but they are easily incorporated after the primary calculation.

Figure 2 shows the current density vs. voltage (J-V) output of a CIGS device. The current density at zero voltage is called **short-circuit current density** J_{sc} and the voltage at zero current is called the **open-circuit voltage** V_{oc} . At some voltage, the product of current and voltage will be maximized; the current density and voltage at this point carry the subscript ‘M’. The **fill factor** ff is then defined as:

$$ff = \frac{P_{max}}{J_{sc} V_{oc}} = \frac{J_M V_M}{J_{sc} V_{oc}} \quad (2.3)$$

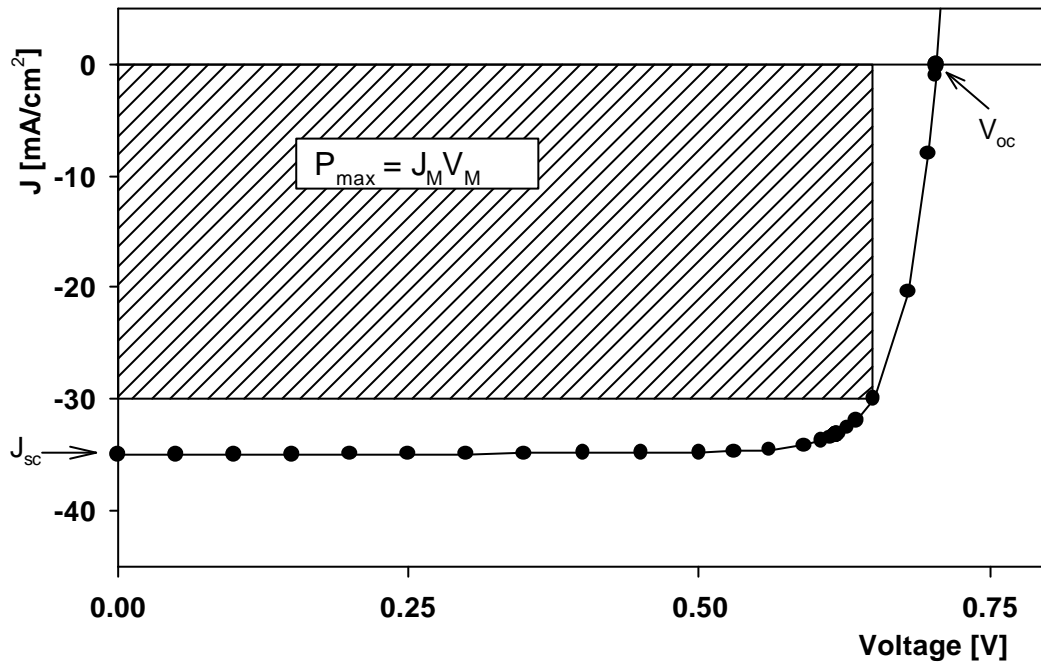


Figure 2: J-V Characteristics with important parameters

To determine the diode quality factor it is helpful to plot J-V data on a logarithmic scale (Figure 3). In general, at least two regions in these plots can be distinguished. The net current is dominated by the recombination current in the lower voltage range and by the ideal diode current at higher voltages [4]. A computer code was written to ensure fast and accurate extraction of the diode quality factor in both areas, labeled “ A_{low} ” and “ A_{high} ” in the upcoming discussion. The extraction is most safely done using the dark

current-voltage curve, since the light curves show a considerable difference in the voltage range below 0.5 V (see Figure 3), due to the change in average collection efficiency caused by the varying width of the space charge region. Some examination of the light quality factor is needed, however, to determine that it is not significantly different from the dark value. Based on Ref. [5], a correction for the light data was calculated that resulted in excellent superposition of the light and dark current-voltage curves. For simplicity, only the dark curves were used to extract diode quality factor in this work.

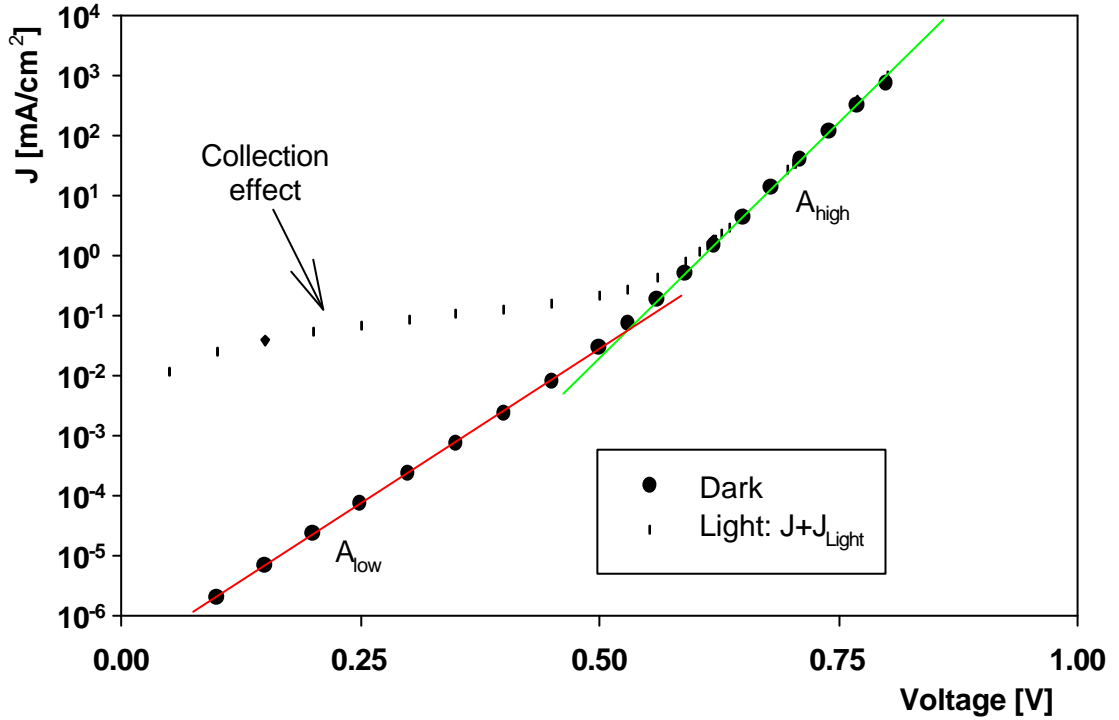


Figure 3: J-V data on a logarithmic scale

The **efficiency h** of a solar cell is defined by:

$$\mathbf{h} = \frac{V_M J_M}{P_{inc}} \quad (2.3)$$

where P_{inc} is the incoming power density. For consistent comparisons, a standard illumination is used in photovoltaic research. Unless otherwise mentioned, all calculations or

measurements used air mass 1.5 (AM1.5) illumination, which is equivalent to cloudless 45° illumination on the earth surface at sea level. AM1.5 delivers a power density $P_{inc} \approx 100 \text{ mW/cm}^2$.

Monochromatic illumination allows the deduction of efficiency for every wavelength. This information is commonly referred to as **quantum efficiency (QE)** or **spectral response (SR)**. The QE of a simulated and an experimental CIGS cell is shown in Figure 4. QE is a function of wavelength and can be written as:

$$QE(\lambda) = \frac{n(\lambda)}{N(\lambda)} \quad (2.4)$$

with $n(\lambda)$ being the number of generated electron-hole pairs that contribute to I_L , and $N(\lambda)$ being the number of incident photons, both measured at a specific wavelength.

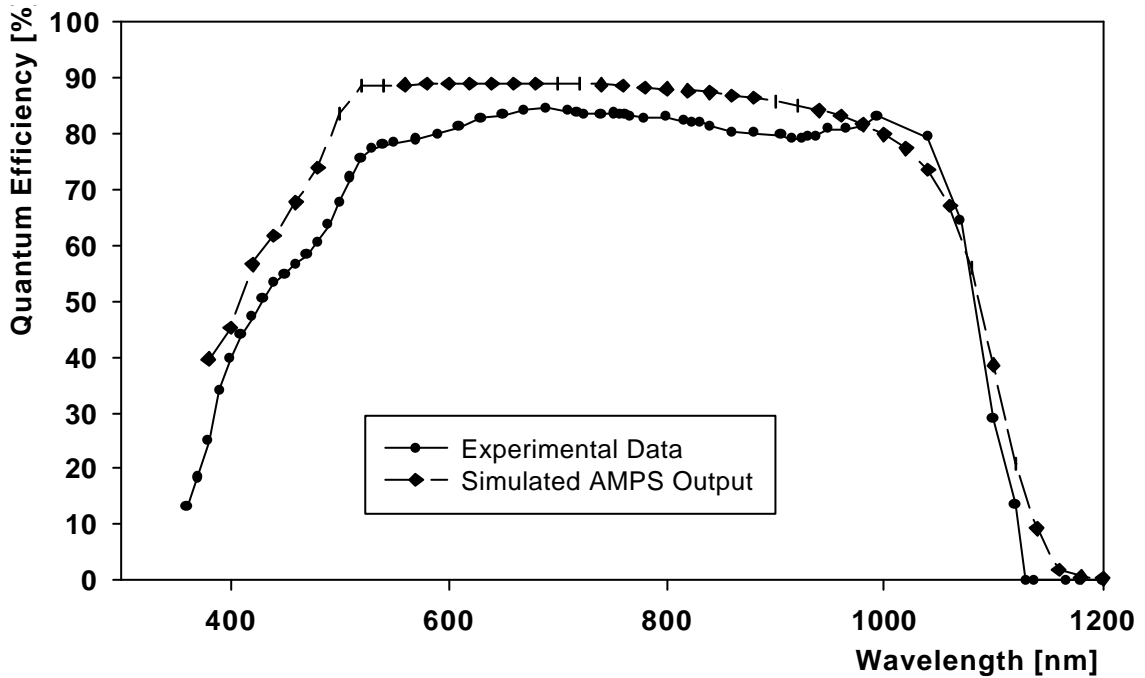


Figure 4: Measured and calculated quantum efficiency

The drop in QE below 520 nm wavelength is caused by the photon absorption in the CdS window layer (band gap $E_G = 2.4 \text{ eV}$). The drop at higher wavelengths ($\sim 1100 \text{ nm}$)

corresponds to the CIGS band gap of $E_G = 1.12$ eV. No collection is seen beyond 1170 nm. The experimental QE curve also shows some optical interference (wiggles in the curve) in the range between 400 nm and 1000 nm. AMPS does not include interference effects and therefore the response will always give a smooth line with a maximum $QE_{\max} = 1 - R_F$, where R_F is a wavelength-independent reflection parameter for the front surface of the cell (for the values used see chapter 3). As with resistive effects, a supplementary calculation can be made to include optical interference.

2.3 Band Offsets

Band offsets, which can considerably influence device performance, are created when different materials are brought together. Traditionally it is assumed that conduction band offsets are determined by the electron affinities of two materials. Figure 5 shows the three-layer structure of a CIGS solar cell where the layers are artificially separated.

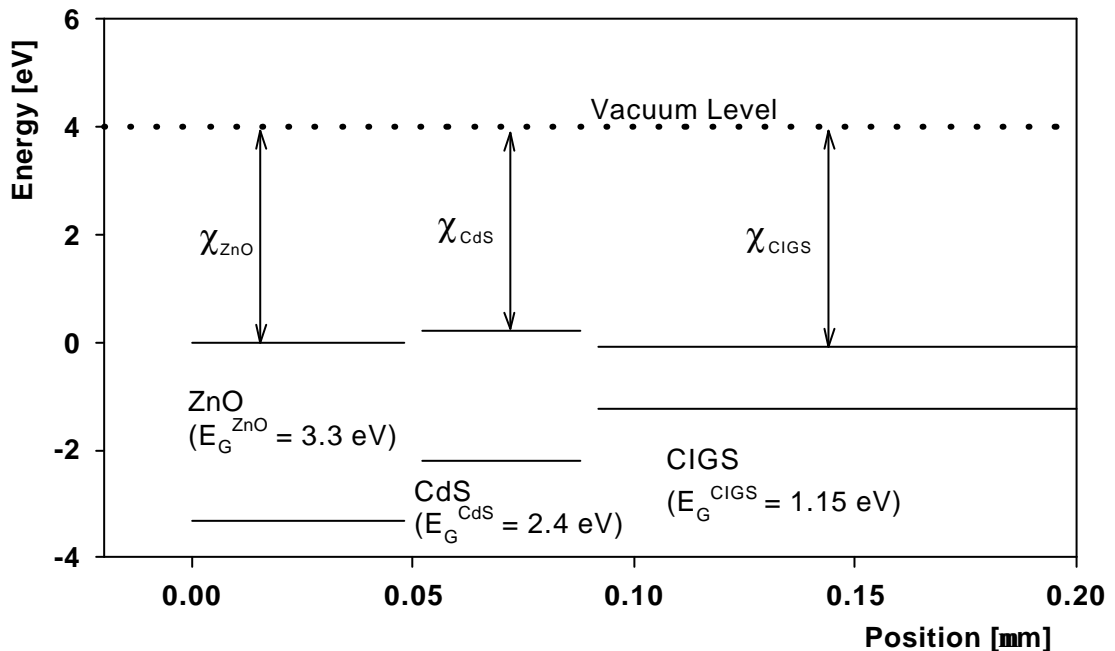


Figure 5: ZnO/CdS/CIGS structure separated. Conduction and valence-band edges shown by solid lines. Zero defined by ZnO conduction band edge.

The electron affinity χ is defined as the energy that it takes to remove an electron that is located at the conduction-band edge of the material:

$$\mathbf{c} = E_{vacuum} - E_C \quad (2.5)$$

When the layers in Figure 5 are joined, a flow of carriers will take place until there exists a single Fermi level throughout the device. In general, this leads to considerable bending of the bands. A resulting band diagram for a CIGS cell in thermodynamic equilibrium is shown in Figure 6. Independent of band bending, illumination, or voltage bias, the band offset at the interface will always be the same, given by the difference of the electron affinities. For the conduction band offsets:

$$\Delta E_{C1} = \mathbf{c}_{CdS} - \mathbf{c}_{ZnO} \quad \Delta E_{C2} = \mathbf{c}_{CIGS} - \mathbf{c}_{CdS} \quad (2.6)$$

and for the valence band offset:

$$\Delta E_{V1} = \mathbf{c}_{ZnO} - \mathbf{c}_{CdS} + (E_G^{ZnO} - E_G^{CdS}) \quad \Delta E_{V2} = \mathbf{c}_{CdS} - \mathbf{c}_{CIGS} + (E_G^{CdS} - E_G^{CIGS}) \quad (2.7)$$

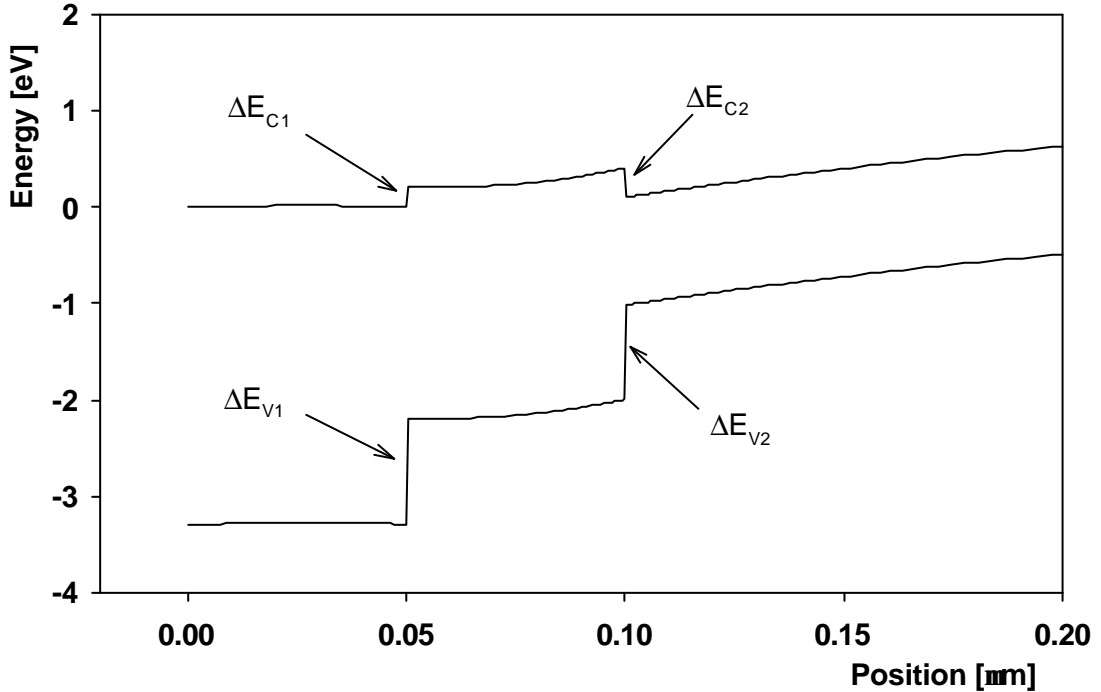


Figure 6 : Band diagram for ZnO/CdS/CIGS structure

The sign of the band offsets is determined by the following rule [6]: ‘...*conduction- and valence-band offsets are positive if neither exceeds the magnitude of the band gap difference (Type I), but one offset must be negative otherwise (Type II).*’ The ZnO/CdS offset is hence Type II and the CdS/CIGS offset Type I. This can also be readily seen by substituting eqn. (2.5) into eqn. (2.6):

$$\Delta E_{V_2} + \Delta E_{C_2} = E_G^{CdS} - E_G^{CIGS} \quad (2.8)$$

and similarly for the ZnO/CdS interface.

Extensive investigation was done by Liu [6] to determine the J_{sc} , V_{oc} , ff, and η dependence on the band offsets. She showed that the conduction band offset could vary from approximately -0.4 eV up to 0.4 eV without major changes in the solar-cell parameters. Exceeding these limits, she reports a major loss in fill factor for $\Delta E_{C_2} < -0.4$ eV and an abrupt loss in short circuit current for $\Delta E_{C_2} > 0.4$ eV. All of these calculations were done assuming the device was at room temperature.

While there exist a variety of methods to measure band offsets (for a list of experimental methods see for example [7]), there is still considerable uncertainty in these numbers. Measurement results commonly do not confirm the band offsets predicted by the electron affinities of the materials. The band offsets depend strongly on the deposition technique and are neither reproducible nor predictable if the structure or process is changed. A good overview on the status on band offsets in CdS/CIS structures can be found in a publication from Wei and Zunger [8]. In their work, the conduction band offset for the CdS/CIS interface is found to be about +0.3 eV based on theoretical calculations, which contradicts the negative offset of -0.28 eV, based on the electron affinities of CdS and CIS. Experimental investigations of the CdS/CIS interface by Schmid et al.

[9] confirmed the positive offset of +0.3 eV. The CIGS typically used, 20% indium replaced by gallium, should not alter these numbers significantly.

In Chapter 3, the effects of the band offsets will be studied using the AMPS software. Chapter 4 applies the results of chapter 3 to the modeling of specific experimental devices, in which the conduction band offset led to significant failure of the light/dark superposition.

Chapter 3

AMPS Modeling – Base Case

This chapter discusses the set-up of the ZnO/CdS/CIGS model with the AMPS software. Input parameters are explained in the context of the base case, which was the baseline for subsequent variational investigations. Input parameters were selected based on experimental data, literature values, theory, or in some cases, reasonable estimates. The base case is partially selected so that no single loss mechanism, i.e. a high number of defects in the CIGS, significantly limits the performance. This however, is often not the case in real devices and therefore, the base case will outperform most experimental devices.

3.1 Description of the Base Case

Three types of parameters are necessary before any AMPS simulation can be started:

- Material properties for each layer, including front and back contact
- Environmental conditions
- Modeling settings: i.e. model type, grid spacing for the numerical calculations, bias voltages for which J-V and QE output should be generated

Material Properties:

The material parameters that define the base case are listed in Table 1. A detailed discussion of these numbers is given in Sections 3.2 - 3.4.

Table 1: Parameters for the base case

General Device Properties			
	Front Surface (x = 0 mm)		Back Surface (x = 3.1 mm)
$\Phi_{b0/L} = E_C - E_F$	0.0 eV		0.9 eV
Surface recombination electrons	10^7 cm/s		10^7 cm/s
Surface recombination holes	10^7 cm/s		10^7 cm/s
Reflectivity	0.1		0.8
Layer Properties			
	ZnO	CdS	CIGS
Width	50 nm	50 nm	3000 nm
Dielectric constant	9.0	10	13.6
Electron mobility	$100 \text{ cm}^2/\text{Vs}$	$100 \text{ cm}^2/\text{Vs}$	$100 \text{ cm}^2/\text{Vs}$
Hole mobility	$25 \text{ cm}^2/\text{Vs}$	$25 \text{ cm}^2/\text{Vs}$	$25 \text{ cm}^2/\text{Vs}$
Carrier density	$N_D = 10^{18} \text{ cm}^{-3}$	$(N_D) = 10^{17} \text{ cm}^{-3*}$	$(N_A) = 2 \times 10^{16} \text{ cm}^{-3*}$
Bandgap	3.3 eV	2.4 eV	1.12 eV
Effective dens. NC	$2.22 \times 10^{18} \text{ cm}^{-3}$	$2.22 \times 10^{18} \text{ cm}^{-3}$	$2.22 \times 10^{18} \text{ cm}^{-3}$
Effective dens. NV	$1.78 \times 10^{19} \text{ cm}^{-3}$	$1.78 \times 10^{19} \text{ cm}^{-3}$	$1.78 \times 10^{19} \text{ cm}^{-3}$
Electron affinity	4.0 eV	3.8 eV	4.1 eV
Defect States			
Gaussian Defects	ZnO	CdS	CIGS
Defect density	$N_{DG} = 10^{17} \text{ cm}^{-3}$	$N_{AG} = 10^{18} \text{ cm}^{-3}$	$N_{DG} = 10^{14} \text{ cm}^{-3}$
Peak energy	midgap	midgap	midgap
Standard deviation	0.1 eV	0.1 eV	0.1 eV
Cross-section elect.	$1.2 \times 10^{12} \text{ cm}^2$	10^{17} cm^2	$5.3 \times 10^{13} \text{ cm}^2$
Cross-section holes	10^{17} cm^2	$9.8 \times 10^{13} \text{ cm}^2$	10^{18} cm^2

* Carrier density is not equal to the parameters N_D or N_A (see discussion Chapter 3.3)

Environmental Conditions:

The illumination is discretely defined (Figure 7). The number of incident photons/(cm^2s) was entered for wavelengths between 0.38 μm and 1.24 μm , with a step size of 0.02 μm . It is unnecessary to specify the illumination spectrum beyond these limits since, as mentioned in chapter 2.2, CIGS solar cells have only measurable quantum

efficiency in the range of 0.35 – 1.2 μm (Figure 4). The discrete spectrum $I_{\text{dis}}(\lambda_i)$ can be calculated from the standard AM1.5 spectrum, $I_{\text{AM1.5}}(\lambda)$, by:

$$I_{\text{dis}}(\lambda_i) = \int_{\lambda_i - 0.01\text{mm}}^{\lambda_i + 0.01\text{mm}} I_{\text{AM1.5}}(\lambda) d\lambda \quad (3.1)$$

where $I_{\text{AM1.5}}(\lambda)$ is given in the units of photons per area*time*wavelength.

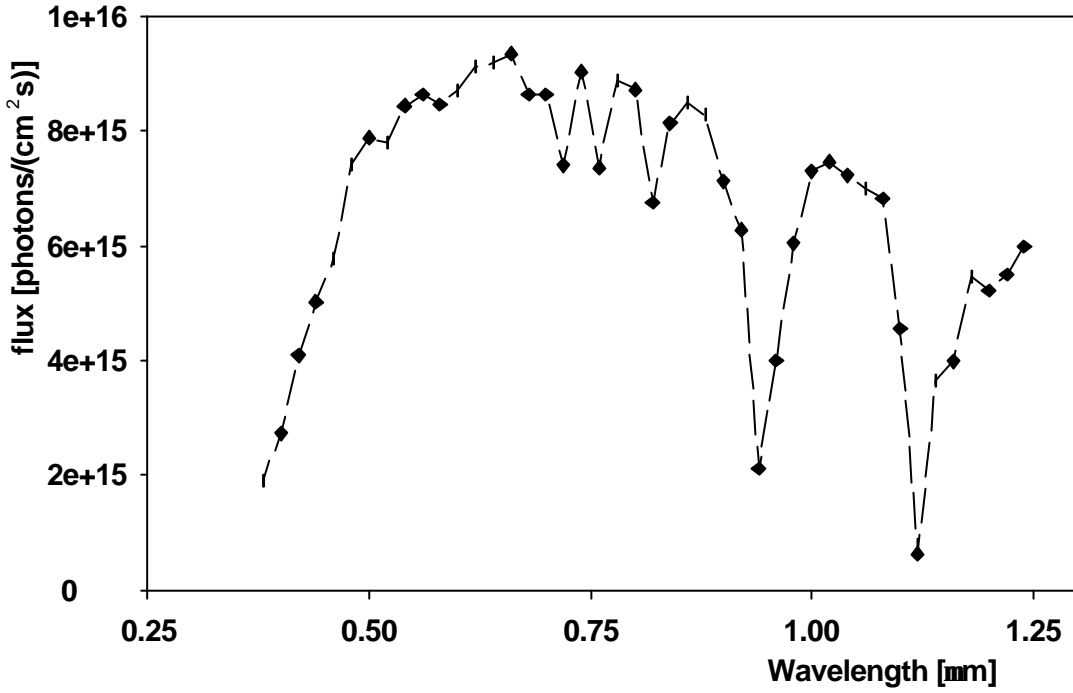


Figure 7: AM1.5 illumination spectrum

The temperature for the base case and for all variations, discussed in Chapter 4, was set to 298 K. Temperature effects and temperature dependences of input parameters are addressed in chapter 4.7.

Modeling Setting:

The AMPS software can operate in two distinct modes: the density of state (DOS) mode or the lifetime mode. A description of both modes can be found in the AMPS

manual [3]; a comparative discussion is found in A.L. Fahrenbruch's work on CdTe solar cells [10]. In essence, the lifetime mode accepts inputs in the form of carrier lifetimes, which are assumed constant, independent of light and voltage bias, and does not address the underlying recombination processes. The DOS mode allows the definition of multiple defect states, using densities, energy distributions, and capture cross-sections. Based on this information recombination current and defect occupancy is calculated using the Shockley-Read-Hall formalism. All modeling done for this work used the DOS mode.

The grid spacing was selected to be denser in the thinner top layers of the device, where more rapid changes are to be expected in the band structure. Selected biases were entered as necessary; by default AMPS calculates QE and band structure for thermodynamic equilibrium, maximum power point, and under open-circuit conditions.

3.2 General Device Properties

Front and Back Contacts

The front and back contacts are solely defined by their work function and the reflectivity of the contact-semiconductor interface: $\Phi_{b0} = 0$ eV pins the conduction band at the Fermi level E_F at $x = 0$ μm (front) and $\Phi_{bL} = 0.9$ eV pins the conduction band 0.9 eV above E_F at $x = L$ (back). These numbers create an ohmic contact at the front and a negligible Schottky Barrier at the back. Strong back barriers are frequently observed in thin-film solar cells, especially cells based on the CdTe compound; however, such effects are not contained in the base case.

Surface Recombination

Interfaces between polycrystalline layers are rich in defect states, generated by lattice mismatch and impurities, that cause recombination current. The parameter used to

describe this recombination current is given in terms of a surface recombination velocity [11]. All numerical calculation for this work used a surface recombination velocity of 10^7 cm/s, which corresponds approximately to the thermal velocity of the electrons.

Front and Back Surface Reflectivity

The front surface reflectivity limits quantum efficiency (as described in Chapter 2.2) and therefore J_{sc} . This parameter is set to 0.1 in order to reflect experimental QE data. The back reflection has only negligible influence on the performance since only few absorbable photons (close to the CIGS band gap) transverse the device and therefore get a chance of being reflected.

3.3 Layer Properties

Thicknesses of the layers are chosen as they are found in typical experimental devices. Dielectric constants and band gaps are common knowledge and can be found in literature or through direct measurement (i.e. QE).

Mobility's and Effective Density of States

The mobility and effective density of states values are essentially unknown. The following arguments were used in the selection of these parameters:

- Mono-crystalline CIGS mobilities have been measured to be $\mu_e = 300$ cm²/Vs for electrons and $\mu_h = 30$ cm²/Vs for holes. Mobilities for polycrystalline materials should be lower than these numbers due to grain boundary effects, but not strongly smaller since the layer thickness is similar to grain size.
- Mobility ratios (μ_e/μ_h) should be similar (assumed equal) to the inverse ratio of effective masses (m_h^*/m_e^*) involved.

- Effective masses were estimated to be $m_e^* = 0.2m_0$ and $m_h^* = 0.8m_0$. Similar numbers can be found in the literature, however there is some spread in the reported values.
- Density of states were calculated from the estimated masses using [11]:

$$N_c = 2 \left(\frac{2\mathbf{p}n_e^*kT}{h^2} \right)^{\frac{3}{2}} \quad N_v = 2 \left(\frac{2\mathbf{p}n_h^*kT}{h^2} \right)^{\frac{3}{2}} \quad (3.2)$$

The same values were used for the ZnO, CdS, and CIGS material.

Carrier Concentrations:

ZnO and CdS layers are designated as n-type materials with high carrier concentrations. CIGS is p-type with a commonly observed carrier concentration. No activation energy is assigned to any of the shallow donor/acceptor levels; full ionization of these is always assumed.

Band Offsets:

Band Offsets in the model are defined via the electron affinities of the different layers using eqn. 2.6 and 2.7. ΔE_{c2} , as defined in Figure 6, was set to 0.3 eV, which was found experimentally [9] and theoretically [8]. ΔE_{c1} is set to -0.2 eV.

Absorption Coefficient:

The absorption coefficient $\alpha(\lambda)$ reflects how strongly light of a specific wavelength λ is absorbed in the material. The optical band gap of the semiconducting material is indirectly defined by $\alpha(\lambda)$. The band gap of $\text{CuIn}_{1-x}\text{Ga}_x\text{Se}_2$ varies with the composition of the material; the absorption curve was shifted in wavelength in order to match the desired band gap energy. $\alpha(\lambda)$ for ZnO, CdS, and CIGS is shown in Figure 8.

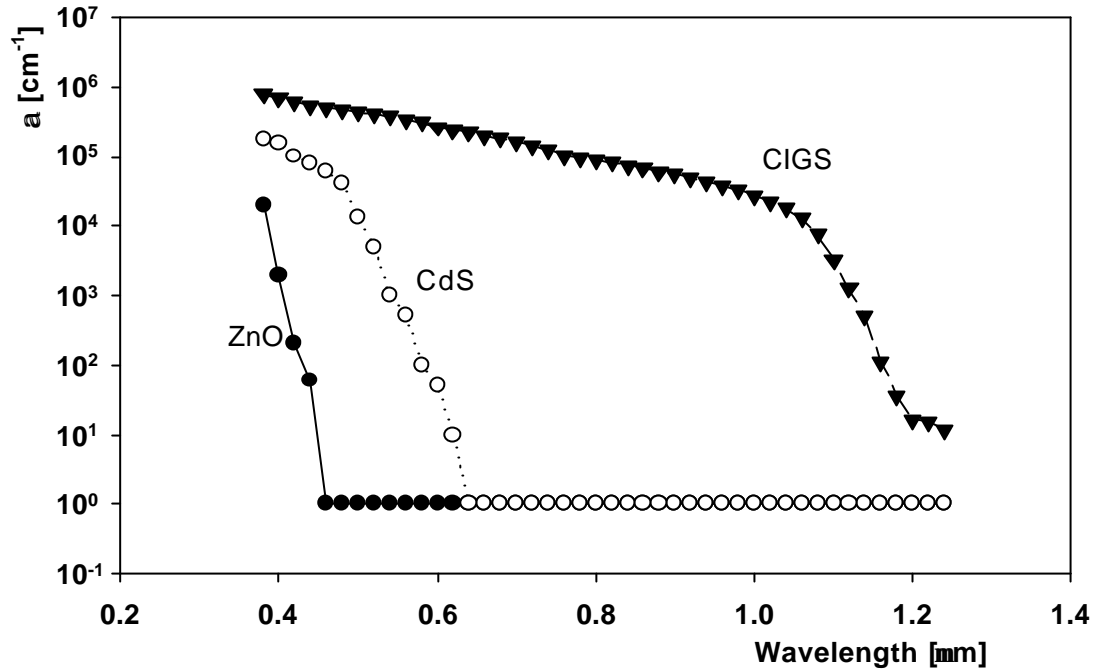


Figure 8: Absorption spectra for ZnO, CdS, and CIGS

3.4 Defect States

AMPS uses the Shockley-Read-Hall recombination model that was introduced in 1952 [12]; a good discussion is found in [13]. This statistical model assumes four possible transitions and assigns transition probabilities to each of them. The following will be discussed in terms of “acceptor-like” defect states, but it similarly applies to “donor-like” states. The allowed transitions are (Figure 9):

For a **neutral acceptor-like** defect:

- 1: Capture of an electron from the conduction band
- 2: Emission of a hole to the valence band

For an **ionized acceptor-like** defect:

- 3: Capture of a hole from the valence band
- 4: Emission of an electron to the conduction band

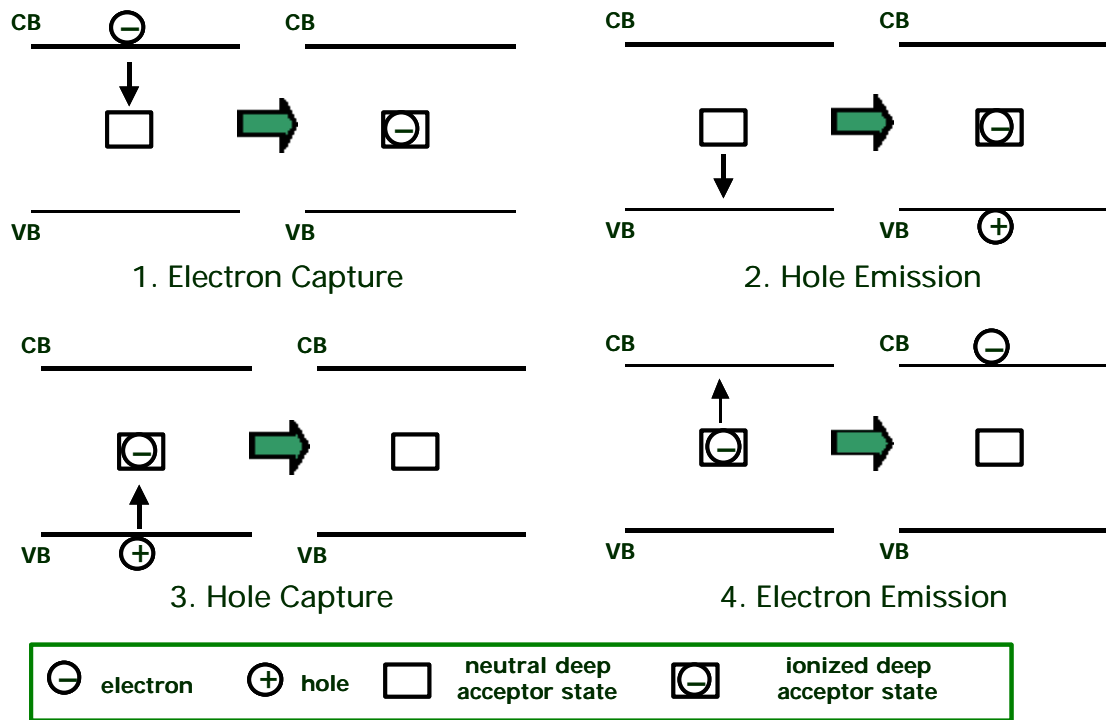


Figure 9: Allowed transitions in the Shockley-Read-Hall model

Transition 2 followed by transition 4 generates an electron-hole pair and transition 1 followed by transition 3 recombines an electron-hole pair. In thermodynamic equilibrium both transitions pairs, (2,4) and (1,3), are equally likely. Under light or voltage bias, the recombination process dominates, since it depends on the increased free carrier concentrations in the valence and conduction band whereas the generation process does not.

In the base case, only a single type of defect was added to each of the three layers, in addition to the shallow donor/acceptor states needed for the desired free carrier concentration (intentional doping). The defects are assumed donor-like in the ZnO and CIGS, and acceptor-like in the CdS. This selection was influenced by what is usually found to be the dominating defect type, characterizing experimental devices.

Defect Ionization and Defect Density

Defects contribute to the space charge, if they become ionized: i.e. a donor-like defect that captures a hole (loses its electron) carries a single positive charge. The probability for an acceptor (donor) defect state to be ionized is given by the Fermi function f_A ($1 - \text{Fermi function} = f_D$):

$$f_A = \frac{1}{1 + \exp\left(\frac{E - E_F}{kT}\right)} \quad f_D = \frac{1}{1 + \exp\left(\frac{E_F - E}{kT}\right)} \quad (3.3)$$

Eqn. 3.3 is only valid in thermodynamic equilibrium; under forward bias, illumination, or both, the Shockley-Read-Model (S-R-H) predicts different probabilities that depend on state populations and capture cross-sections of the defects [3].

For example in the CIGS p-layer, all donor-type defects are assumed ionized, therefore, the acceptor density entered into the model equals the desired carrier concentration plus the hole concentration necessary to ionize the deep states, $N_A = 2.01 \times 10^{16} \text{ cm}^{-3}$. Similarly, the density of shallow donor states in the CdS layer needs to be adjusted. The defect density for the CdS layers is dictated by the QE loss in the wavelength range below 520 nm. The value chosen (10^{18} cm^{-3}) is a factor of 10 higher than the carrier concentration (10^{17} cm^{-3}). This is summarized in Table 2.

Table 2: Defect Densities

Layer	Desired Carrier Concentration	Ionized Deep States	Necessary Input Parameter
ZnO	10^{18} cm^{-3}	-	$N_D = 10^{18} \text{ cm}^{-3}$
CdS	10^{17} cm^{-3}	$N_{AG} = 10^{18} \text{ cm}^{-3}$	$N_D = 1.1 \times 10^{18} \text{ cm}^{-3}$
CIGS	$2 \times 10^{16} \text{ cm}^{-3}$	$N_{DG} = 10^{14} \text{ cm}^{-3}$	$N_A = 2.01 \times 10^{16} \text{ cm}^{-3}$

Defect Distributions

In all layers, the defects (donor-like = d, acceptor-like = a) are assumed to have a gaussian distribution around their peak energy, $E_{P(d,a)}$ of the form [3]:

$$g_{d,a}(E) = G_{d,a} \exp\left\{-\frac{1}{2}\left[\frac{(E - E_{P(d,a)})^2}{\sigma_{d,a}^2}\right]\right\} \quad (3.4)$$

$G_{d,a}$ is the defect densities/energy at $E = E_{P(d,a)}$ and $\sigma_{d,a}$ is the spread of the distribution (standard deviation). $g_{d,a}(E)$ integrated over all energy will give N_{DG} or N_{AG} , the total defect density, which is the AMPS input parameter.

Cross-Sections

Transition 1, in Figure 9, represents a “neutral transition” since an electron is captured into a neutral trap. Transition 3 represents an “attractive transition” since the hole is coulomb attracted by the negatively charged trap state. Similarly, electron cross-sections for donor-like states are attractive and hole cross-sections for donor-like states are neutral. The range of plausible values for cross-sections is discussed in reference [7].

Cross-sections were assigned as follows:

- Attractive cross-sections correspond to a radius at which the coulomb potential energy of the electron in the field of the charged trap equals kT:

$$s_{att} = \frac{q^4}{16\pi\epsilon_s^2 k^2 T^2} \approx 10^{-13} - 10^{-12} \text{ cm}^2 \quad (3.5)$$

q elementary charge, k Boltzmann constant, T temperature, ϵ_s permittivity

- Neutral cross-sections can range between 10^{-20} to 10^{-15} cm^2 , the latter number corresponds to the physical size of an atom. Smaller numbers are necessary to account for quantum mechanical transition probabilities, i.e. forbidden transitions

will have very small, zero approaching, cross-section. 10^{-17} cm^2 was chosen as a default value for the ZnO and CdS layer. However, in the CIGS layer, 10^{-18} cm^2 is used to limit the recombination current even further and to achieve a more ideal device.

Tail States

See chapter 4.5.

3.5 Modeling Results for the Base Case

Modeling results for the base case are shown in Figure 10. Top left (a) shows light and dark J-V plots ($J_{sc} = 34.5 \text{ mA/cm}^2$, $V_{oc} = 0.65 \text{ mV}$, $ff = 83\%$, $\eta = 18.6\%$) with a reasonable superposition in the area of interest: $J_{light}(V) - J_{dark}(V) - J_L$.

The efficiency is very similar to the best cells that have been made to date. Diode quality factors deduced from the logarithmic dark J-V plot (b) are $A_{low} = 1.27$ and $A_{high} = 1.07$. Quantum efficiency (c) shows a peak response of $(1 - R_f) * 100\% = 90\%$ and falls off in the range below 520 nm due to absorption and recombination in the CdS layer. The band structure (d) is shown in thermodynamic equilibrium (dark, 0 V bias) with the constant Fermi level E_f throughout the device. The pinning of the metal contact at $x = 0 \text{ }\mu\text{m}$ and $x = L$ is clearly visible; note the break on the x-axis and the inversion of the p-type absorber close to the junction.

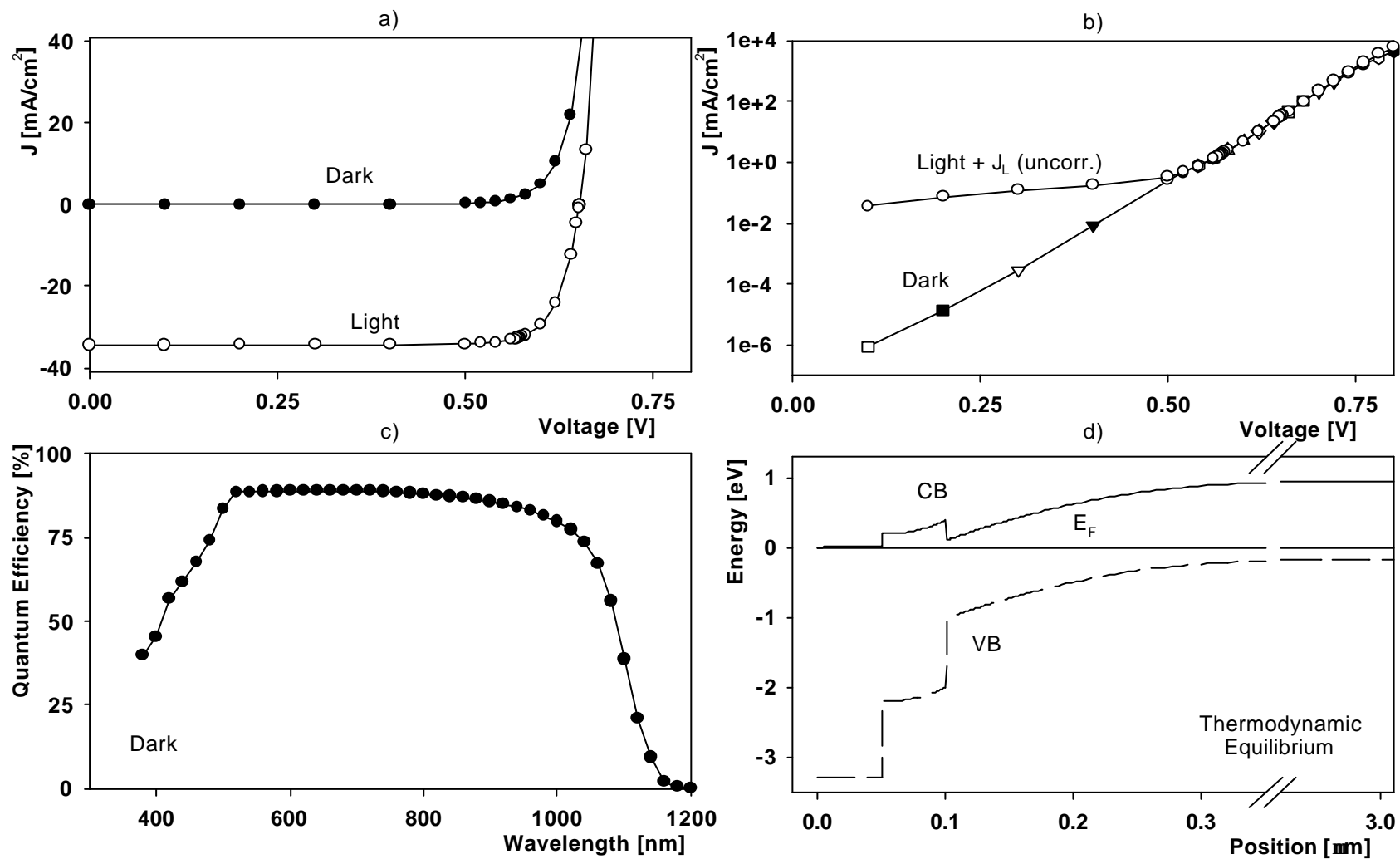


Figure 10: Base case results

Chapter 4

AMPS Modeling – Variational Cases

4.1 Parameter Variations vs. Modeling Output (JV and QE)

Table 4 (page 25) shows all the parameter variations that were performed on the base case. Output parameters are determined as described in Chapter 2.2; QE changes are addressed as “blue” ($\lambda = 380$ nm) and “red” ($\lambda = 1000$ nm). Diode quality factors were extracted in the range 0 V – 0.4 V for A_{low} and around V_{oc} for A_{high} . The changed parameters, the range over which they were varied, and the default values are given in the first three columns. Column 4 to 10 shows the dependence of the output parameters on the input parameter. The changes are indicated using the following rules:

- “+”, “+ +”, or “+ + +”, if an input parameter **increase** creates a **positive** change of the output parameter (values see Table 3).
- “-“, “- -“, or “- - -“, if an input parameter **increase** creates a **negative** change of the output parameter (values see Table 3).
- “±”, “±±”, or “±±±”, if neither one of the above selection rules is applicable.
- “0”, if the changes are negligible.

Table 3: Magnitude of changes

	ΔJ_{sc} [mA/cm ²]	ΔV_{oc} [V]	Δff [%]	A	ΔQE [%]
0	< 0.1	< 0.005	< 0.5	< 0.05	< 0.5
+ / -	< ± 1	< ± 0.02	< ± 2	< ± 0.2	< ± 3
+ + / - -	< ± 3	< ± 0.05	< ± 5	< ± 0.5	< ± 15
+ + + / - - -	> ± 3	> ± 0.05	> ± 5	> ± 0.5	> ± 15

Table 4: Variations on the base case

	Range	Default	DJsc [mA/cm ²]	DV _{oc} [V]	Dff [%]	DA _{low}	DA _{high}	DQE blue [%]	DQE red [%]
CdS									
Carrier density [cm ⁻³]	0* - 3x10 ¹⁷	10 ¹⁷	0	0	0	0	-	0	+
N _C *N _V [cm ⁻⁶]	3x10 ³⁶ -3x10 ³⁸	4x10 ³⁷	0	0	0	0	-	-	0
Hole mobility [cm ² /Vs]	1 - 100	25	+	0	0	0	0	++	0
Defect density N _{AG} [cm ⁻³]	10 ¹⁶ - 10 ¹⁹	10 ¹⁸	--	0	0	0	0	---	0
Width [nm]	30 - 80	50	-	0	0	0	0	---	0
CIGS – Basic Properties									
Carrier density [cm ⁻³]	10 ¹⁵ - 10 ¹⁷	2x10 ¹⁶	--	+++	±	+	+	+	---
N _C *N _V [cm ⁻⁶]	3x10 ³⁶ -3x10 ³⁸	4x10 ³⁷	0	---	-	--	+	+	0
Elec. mobility [cm ² /Vs]	5 - 300	100	+	---	-	--	0	0	+
CIGS – Gaussian Defect States									
Defect density [cm ⁻³]	10 ¹³ - 10 ¹⁶	10 ¹⁴	---	--	---	++	+++	0	---
Peak energy [eV]	0.15 – 0.9	0.58	±	0	0	±±	±	0	±±
Standard deviation [eV]	0.02 – 0.5	0.1	+	0	0	±	0	0	+
Cross-section elec. [cm ²]	5.3x10 ⁻¹³ – 10 ⁻¹⁶	5.3x10 ⁻¹³	-	0	0	++	+	0	--
Cross-section holes [cm ²]	10 ⁻¹⁵ – 10 ⁻²⁰	10 ⁻¹⁸	--	--	--	+++	++	0	--
CIGS – Tail States (d = donor-like states, a = acceptor-like states)									
Density (d) [cm ⁻³ eV ⁻¹]	10 ¹⁴ - 10 ¹⁹	0	--	--	--	-	0	0	--
Density (a.) [cm ⁻³ eV ⁻¹]	10 ¹⁴ - 10 ¹⁹	0	-	--	-	0	0	0	-
Band Offsets – Electron Affinities									
Barrier shift, ΔE _{C1/2} [eV]	(-0.1) - (+0.2)	0	-	0	+	0	(-)**	--	+
ΔE _{C2} [eV]	0.2 - 0.7	0.3	---	++	---	(+)**	(+)**	++	-
Others									
T [K]	268 – 328	298	0	---	--	--	0	0	+
* N _D = N _{AG} ; free carrier concentration equals concentration of neutral defect states									
** highly irregular changes, see discussion									

The list of variations is not comprehensive, but it contains most of the significant parameters. The range of parameter variations is selected intuitively, based on experience, but limited somewhat in cases where experimental values are available.

4.2 CdS

Changes in the CdS layer influence the J-V and QE curves, since there exists considerable absorption of photons ($E_{\text{photon}} > E_G^{\text{CdS}} = 2.4 \text{ eV}$) in this layer. An increased thickness leads to stronger absorption and therefore to higher loss in the blue QE; higher number of defects causes a stronger recombination of the generated carriers in the CdS layer, again decreasing the blue QE. However, most of the photons in the AM1.5 spectrum are contained in the range above 520 nm, and J_{sc} changes are therefore limited.

In homojunction diodes (i.e. Si) the diode characteristics depend on the material properties of the n-type and the p-type layer. In CIGS solar cells however, the p-type material (the absorber) plays the dominant role. Effective density of states and minority carrier (hole) mobility in the CdS are of almost no relevance to the photovoltaic operation.

4.3 CIGS – Basic Properties

The carrier density N_A in the CIGS absorber can be determined from capacitance-voltage measurements. The changes induced by N_A variations are easily understood looking at the basic diode model:

$$V_{oc} = \frac{kT}{q} \ln \left(\frac{I_L}{I_0} + 1 \right) \quad I_0 = A \left(\frac{qD_e n_i^2}{L_e N_A} + \frac{qD_h n_i^2}{L_h N_D} \right) \quad (4.1)$$

Increasing N_A lowers the saturation current and therefore increases V_{oc} . The changes in QE and J_{sc} are induced by the change in depletion width. Since the red photons are absorbed deeper in the material, the electrons created there depend more strongly on diffusion effects to be effectively collected.

The effective densities of states for single-crystal material are fairly well known, since they follow from measured effective masses. Values for polycrystalline material should be similar. The results are only listed in terms of the product N_C*N_V , since this quantity determines the intrinsic density n_i . Again, the changes in V_{oc} are apparent using Eqn. 4.1.

The electron mobility that is used was chosen to be a factor of three smaller than the value for crystalline material. The variations show that V_{oc} varies greatly with the minority carrier mobility. The mobility's relate to the diffusion coefficients using the Einstein relations:

$$D_h = \frac{kT}{q} m_h \qquad D_e = \frac{kT}{q} m_e \qquad (4.2)$$

Therefore, an increase in electron mobility μ_e increases I_0 and lowers V_{oc} . Note that D_h in eqn. 4.1 is the hole diffusion coefficient in the CdS layer, not the CIGS layer.

4.4 CIGS - Defect States

The output parameters depend strongly on the number of defects and their capture cross-sections. The peak energy and distribution of deep defects, however, have relatively minor influence on performance. Extreme values for width or peak energy do lead to small changes in the lower quality factor; this is attributed to a change in occupancy of the defect states close to the Fermi level and a resulting change in the band structure.

Increasing the number of defect states introduces additional recombination centers and additional space charge. The space charge introduced is compensated by adjusting the shallow acceptor density to keep the carrier concentration fixed (see Section 3.4). Output for various defect densities is shown in Figure 11. Dark and light J-V (a) show significant changes in voltage and fill factor. Up to a density of 10^{14} cm^{-3} voltage and ff remain approximately constant, but beyond 10^{14} cm^{-3} V_{oc} and ff decrease rapidly (c). The base case was intentionally set-up to be in the lower defect density regime to make variations in other parameters more conclusive. In the logarithmic plot (b), it is apparent that the region that is recombination current dominated extends to higher voltages with increased defect density. The diode quality factors, deduced from the dark J-V plots (d), show that A_{low} remains approximately constant, which is also apparent from the parallel J-V-curves in (b), whereas A_{high} increases with N_{DG} .

The **hole** capture cross-section, σ_p , has similar influences on the results as the defect density, since the capture of a hole (transition 3, Chapter 3.4) seems to be the limiting step in the recombination. The probability of capturing a hole into a neutral donor state is given by [12]:

$$r_{hc} = v_{th} \sigma_p p N_{DG} f_A \quad (4.3)$$

where $N_{DG} f_A$ is the number of neutral donor-like defects, p is the free hole concentration and v_{th} the thermal velocity of electrons. From (4.3) it is obvious that σ_p and N_{DG} have a similar effect on the recombination process, i.e. increasing density of increasing cross-section has the same effect.

The **electron** capture cross-section dependence is different. Since the default value is so large, it is not generally the limiting step in the recombination, and the results

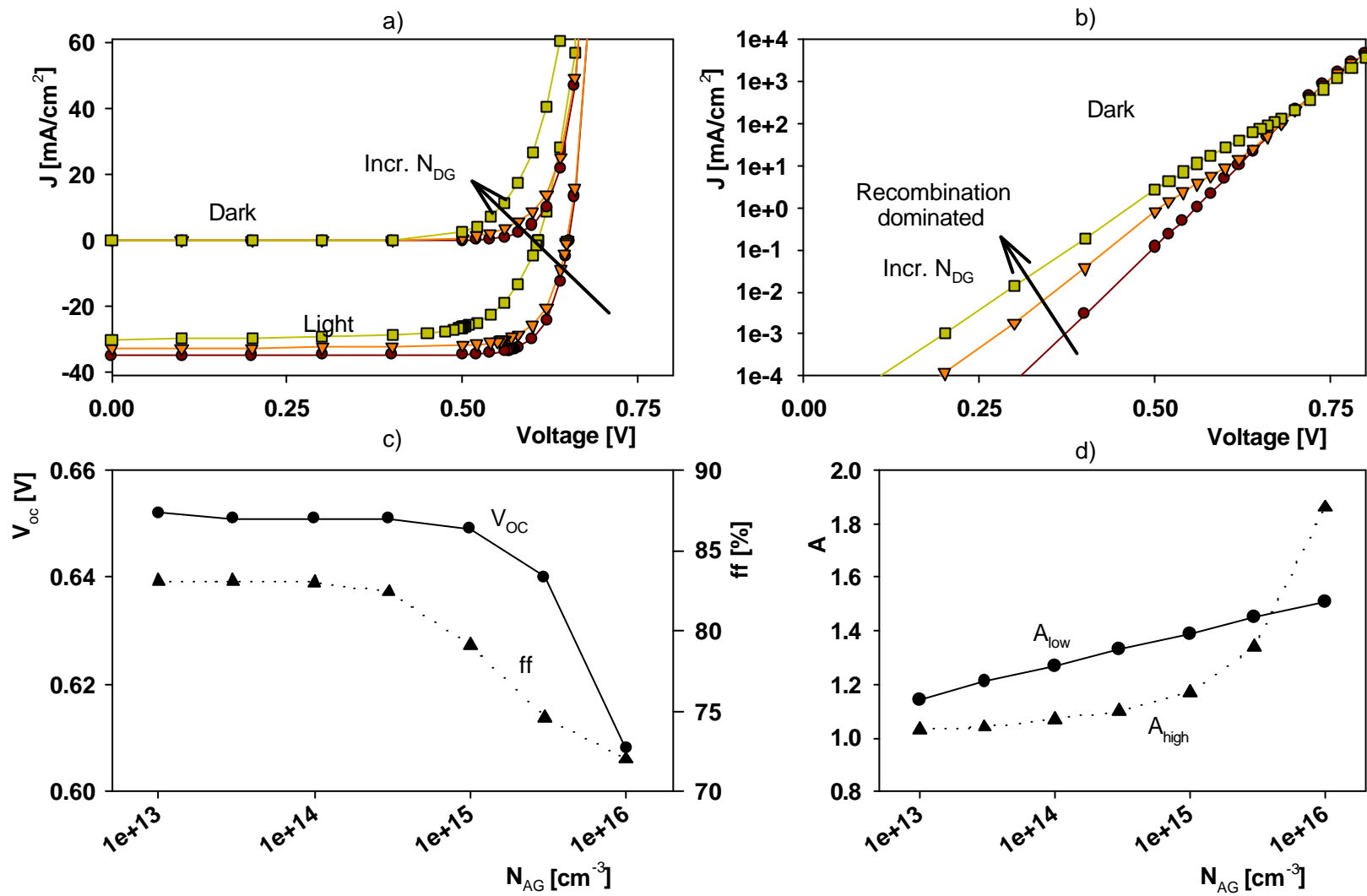


Figure 11: Impact on cell performance with variations in CIGS defect density

are only changed when there is a very low electron concentration in the CIGS, at low voltage in the dark. Then transition 1, the capture of an electron, becomes the limiting process.

4.5 CIGS – Tail States

Tail states are additional donor-like (acceptor-like) states below (above) the conduction (valence) band edge with a density that falls off exponentially with the distance from the band edge. The effects of band tails appeared to be very limited and therefore they were omitted in the base case. This was done practically by setting the density to $1 \text{ cm}^{-3} \text{ eV}^{-1}$. For the variational cases, the cross-sections were selected equally as for the gaussian defect states. The characteristic energy was set to 0.01 eV. The defect density/energy is given by (here for donor-like states):

$$G_D(E) = G_{DO} \exp\left(-\frac{E - E_V}{E_D}\right) \quad (4.4)$$

The total number of introduced defects depends on the defect density/energy at the band edge (G_{DO} , this is the parameter listed in Table 4) and the characteristic energy (E_D). With the given $E_D = 0.01 \text{ eV}$, and $G_{DO} = 10^{18} \text{ cm}^{-3} \text{ eV}^{-1}$ this results in a total number of defects:

$$\int G_D(E) dE = \int_0^{E_G} 10^{18} \text{ cm}^{-3} \exp\left(-\frac{E}{0.01 \text{ eV}}\right) \cong 10^{16} \text{ cm}^{-3} \quad (4.5)$$

which is comparable to the carrier density and two orders of magnitude above the gaussian defect density N_{DG} . These tail states seem to have only weak effect on the device performance unless their total density becomes several magnitudes larger than N_{AG} ($G_{DO} \cong 10^{18} - 10^{19} \text{ cm}^{-3} \text{ eV}^{-1}$).

4.6 Band Offsets – Electron Affinities

Barrier Shift – Equal changes in ΔE_{C1} and ΔE_{C2}

Changing χ_{CdS} shifts the barrier in the conduction band up and down. It keeps the same shape for all values; all four band offsets change (see Table 5). All light curves are similar, whereas the turn up in the dark curves is pushed to higher voltages (Figure 12).

Table 5: Barrier shifts variations

χ_{CdS} [eV]	ΔE_{C1} [eV]	ΔE_{C2} [eV]
3.9	- 0.1	0.2
3.8	- 0.2	0.3
3.7	- 0.3	0.4
3.65	- 0.35	0.45
3.6	- 0.4	0.5

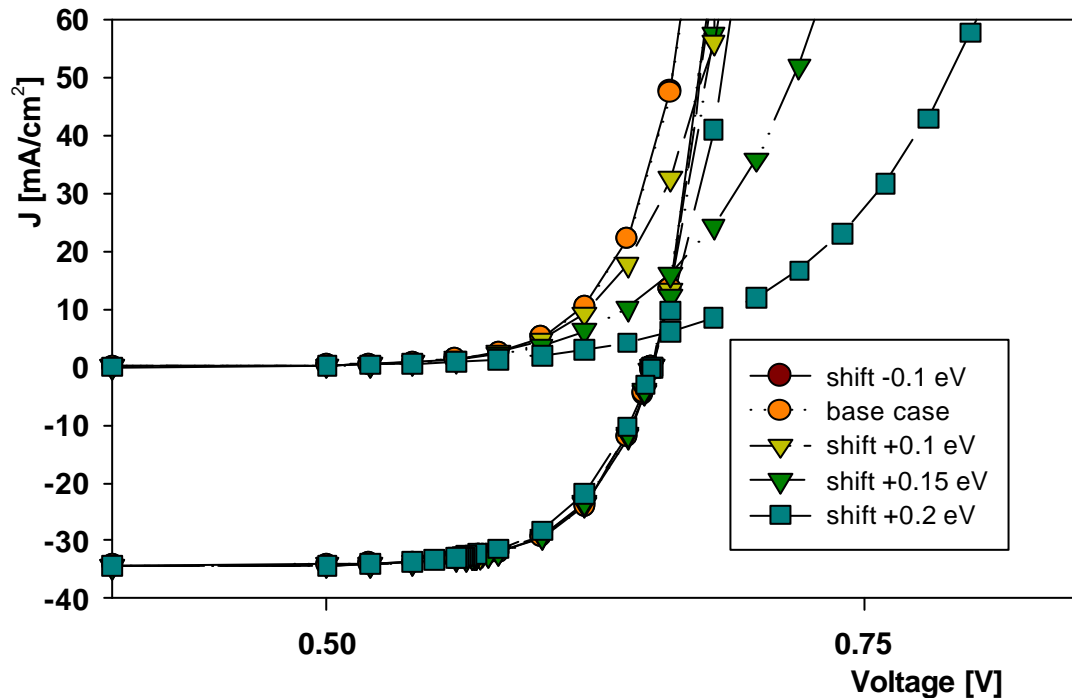


Figure 12: Variations in J-V due to electron affinity of the CdS

The cross-over between light and dark J-V curves increases with increased barrier height. This effect of increasing non-superposition will be used and investigated further in Chapter 5.

Electron Affinity χ_{CIGS}

Changing χ_{CIGS} varies only ΔE_{C2} at the CdS/CIGS interface. J-V light and dark curves for ΔE_{C2} variations between 0.1 and 0.6 eV are shown in Figure 13. Offsets up to 0.4 eV create only minor changes; offsets around 0.5 eV create a voltage shift in the dark, whereas the light curve is still well behaved.

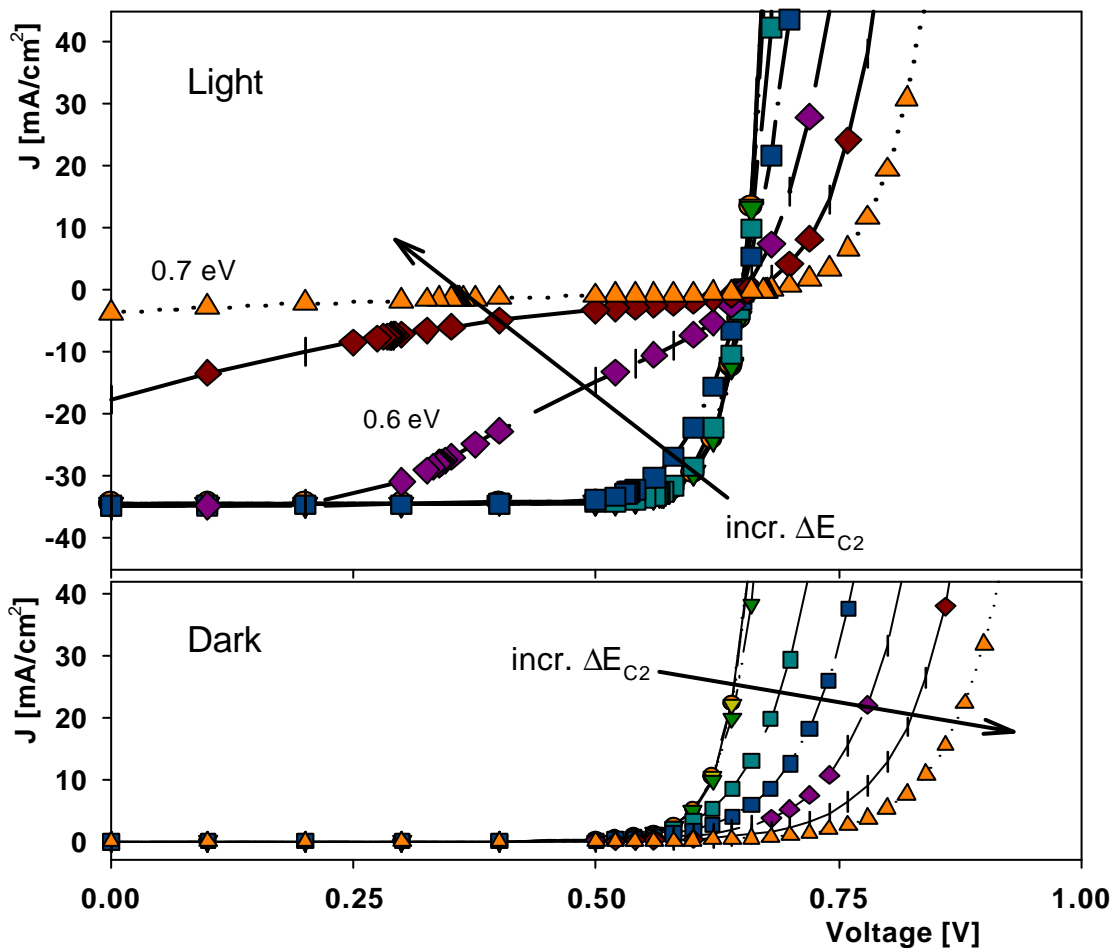


Figure 13: Variations in J-V due to the electron affinity of CIGS

For very high barriers, 0.6 eV and above, the light curve is heavily distorted. This type of distortion is often observed in CIGS solar cells and referred to as the “red kink” effect [14]-[15]. This designation was introduced since this effect is often seen using red light illumination, but it completely disappears under white light.

Both types of barrier variations show that it is possible to induce a change in dark J-V without affecting light J-V. The mechanism generating this strong cross-over will be further investigated in Chapter 5.

4.7 Temperature

Table 6 summarizes the temperature dependent parameters and their values in the range of 238K – 338K. These temperature dependences are contained in their definitions given by Eqn. 3.2 and 3.5. All other parameters are assumed temperature independent.

Table 6: Temperature dependent parameters and their values for T = 238K – 328K

T [K]	N_C [cm^{-3}]	N_V [cm^{-3}]	$\sigma_n(\text{ZnO})$	$\sigma_p(\text{CdS})$	$\sigma_n(\text{CIGS})$
238	1.58E+18	1.27E+19	1.90E-12	1.54E-12	8.33E-13
268	1.89E+18	1.51E+19	1.50E-12	1.21E-12	6.57E-13
278	2.00E+18	1.60E+19	1.39E-12	1.13E-12	6.10E-13
288	2.11E+18	1.69E+19	1.30E-12	1.05E-12	5.69E-13
298	2.22E+18	1.78E+19	1.21E-12	9.82E-13	5.31E-13
308	2.33E+18	1.87E+19	1.14E-12	9.20E-13	4.97E-13
318	2.45E+18	1.96E+19	1.07E-12	8.63E-13	4.66E-13
328	2.56E+18	2.05E+19	1.00E-12	8.11E-13	4.38E-13

Other parameters that may show a temperature dependence are the band gap of the semiconductors and electron and hole mobility. However, sufficient data on these numbers is not available. The variations in Chapter 4.3 showed that changes in mobility on the order of 10-20% should not affect modeling results considerably. Band gap variations would lead to voltage shifts, most likely on the order of 10-20 mV or below, in a temperature range of 60 K.

Calculations in the temperature range 268 K – 338 K, a reasonable range of operating temperatures for real solar cells, show that V_{oc} decreases at a rate of -1.9 mV/K. Diode quality factor A_{high} is constant and A_{low} increased with decreasing Temperature (1.16 at $T = 328$ K, 1.44 at $T = 268$ K). This suggests that at low temperature the recombination current becomes more significant. J_{sc} is constant.

Chapter 5

Modeling of an Experimental Device

Characterization recently performed of experimental devices supplied by the Institute of Energy Conversion (IEC) at the University of Delaware showed strong light/dark non-superposition. The explanation for this effect, confirmed by modeling results, is a secondary barrier produced by the CdS/CIGS conduction band offset and altered by photogeneration in the CdS. This chapter will discuss (a) when to expect such an effect to be significant, (b) why the effect becomes more pronounced at low temperatures, (c) how the effect varies with light intensity and wavelength, and (d) how it evolves to the extreme manifestation known historically as the "red kink".

5.1 Description of the IEC Device

The characterization performed at Colorado State University on samples supplied by IEC included measurements of quantum efficiency (QE), capacitance-frequency, capacitance-voltage (CV), and current-voltage (J-V). J-V was measured at different temperatures (T) varying from 238 K to 308 K (J-V-T). According to the CV measurements, taken at 100 kHz, the carrier density in the CIGS absorber is $1-2 \times 10^{16} \text{ cm}^{-3}$. QE data suggests a band gap (30% response) of about 1.12 eV and shows a maximum response of 85 %. For wavelengths below 500 nm, the absorption in the CdS layer reduces the spectral response considerably. Light and dark J-V data is shown in Figure 14 for temperatures 238 K, 268 K, and 298 K. There is strong cross-over, or non-superposition,

between dark and light curves, and the cross-over increases with decreasing temperature. The temperature progression of the open-circuit voltage is -1.8 mV/K. J-V curves in the dark are shifted to higher voltages and they show stronger temperature dependence. The voltage in the dark, measured at a current density equal to the light-induced current density J_L , changes at a rate of -3.3 mV/K.

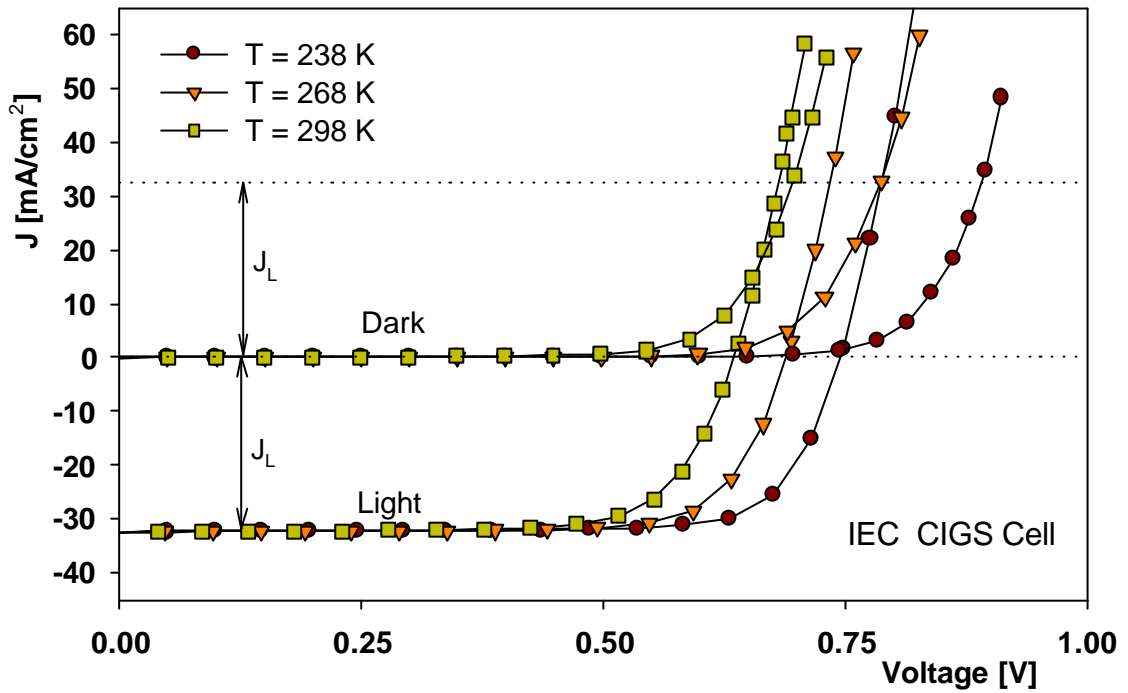


Figure 14: Experimental J-V-T data

The frequently observed “rollover” effect did not appear in this sample within the measured temperature range, suggesting there is no strong secondary reverse diode originating from a non-ohmic back contact. From the J-V data a series resistance of about $0.5 \pm 0.1 \Omega\text{-cm}^2$ was extracted. Quality factors for this device varied from 2.0 at 238 K to 1.6 at 298 K; the “ AkT ” product remained approximately constant at 41 ± 1 meV suggesting that the current transport may be limited by a tunneling process [7].

5.2 Modeling: Best Fit for the IEC Device

Based on the dependences derived in Chapter 4, the AMPS model was altered to fit the IEC device. A reasonably good fit was achieved making the changes listed in Table 7. The changes in electron affinity lead to band offsets $\Delta E_{C1} = -0.2$ eV and $\Delta E_{C2} = 0.4$ eV. The increase in ΔE_{C2} caused the dark J-V curves to shift to higher voltages without affecting the light curves. This introduces a strong non-superposition into the model.

Table 7: Changes from the base case

Parameter		Base case	Best fit
Electron affinity	χ_{CIGS}	4.1 eV	4.2 eV
Width	W_{CdS}	50 nm	40 nm
Reflectivity front surface	R_F	0.1	0.144
Hole cross-section - CIGS		10^{-18} cm^2	10^{-17} cm^2
Carrier density - CdS		10^{17} cm^{-3}	10^{16} cm^{-3}
Series resistance	R_S	$0 \text{ } \Omega\text{cm}^2$	$0.5 \text{ } \Omega\text{cm}^2$

The width of the CdS layer was adjusted to the physical thickness of the deposited layer. Reflectivity at the front surface was adjusted to match the QE and J_{sc} of the experimental data. Increased capture cross-section improved the match in diode quality factors, especially in the high voltage region (A_{high}). Diode quality factor at low voltages cannot be measured with sufficient accuracy experimentally, since the involved currents are extremely small. The decreased effective carrier density of 10^{16} cm^{-3} (N_D is set to $1.01 \times 10^{18} \text{ cm}^{-3}$) leads to a stronger band bending, shifting the barrier, which is generated by the band offsets, up. In addition, according to IEC, there is some evidence that the carrier concentration in the CdS is relatively low. Since the experimental device shows some evidence of series resistance, this was added to the modeling results by changing the voltages V to V' :

$$V' = V + J(V)R_S \quad (5.1)$$

where $J(V)$ is the measured current density at V and R_S the series resistance in $[\Omega\text{-cm}^2]$.

Resulting J-V data is shown in Figure 15 together with the experimental data for temperatures 238 K, 268 K, and 298 K. The fits show the correct temperature progression in the light and the dark. Fits in the dark are good; the fill factor in the light is somewhat high. Considering the simplicity of the model (3 layers, only one defect type/layer) the overall agreement is quite good.

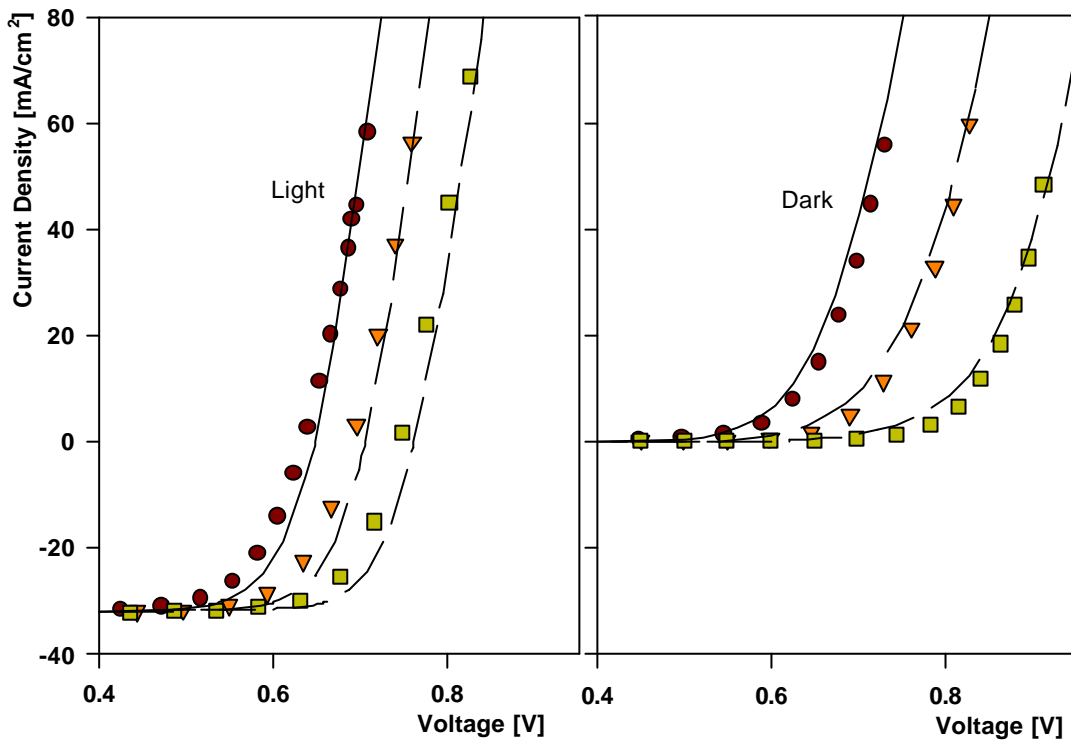


Figure 15: Best fit (lines) with experimental (symbols) J-V-T data at 238 K, 268 K, 298 K

A comparison of J_{sc} , V_{oc} , ff, and the temperature progressions is given in Table 8. Experimental and best fit quantum efficiency is given in Figure 16.

Table 8: Best fit and experimental device in comparison

	J_{sc}	V_{oc}	ff	$\Delta V/\Delta T$ dark	$\Delta V/\Delta T$ light
IEC	-32.4 mA/cm^2	0.635 V	74%	-3.3 mV/K	-1.8 mV/K
Best Fit	-32.4 mA/cm^2	0.651 V	79%	-3.4 mV/K	-1.9 mV/K

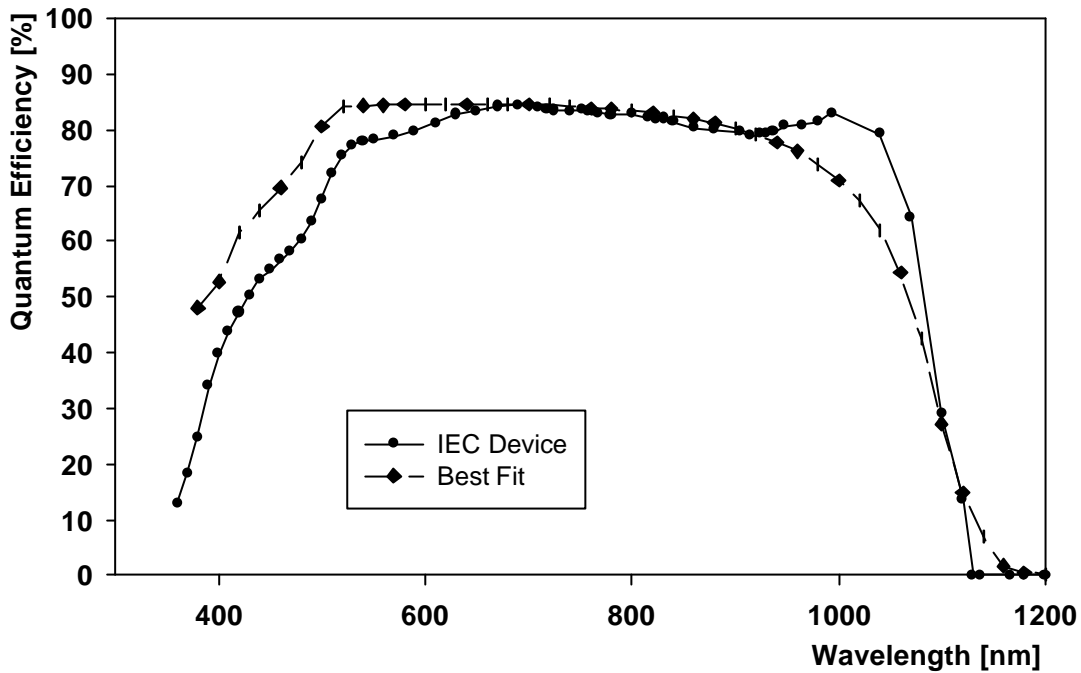


Figure 16: Best fit with experimental QE

The quantum efficiency comparison does show a decent match. While the band gap and maximum response find very good agreement, there is a discrepancy in the blue range below 600 nm and in the red range around 1050 nm. Neither of these discrepancies can be resolved in AMPS. The error in the blue range results mostly from optical interference effects in the top layer of the device, which are not handled in AMPS. Whatever causes the quantum efficiency to raise in the 1050 nm range is not possible to model with the three layer device structure. Changes in this range might be accomplished by introducing:

- a high defect interface layer between CdS and CIGS
- a change in the absorption curve; however a turn up in the absorption curve at high wavelength, close to the band edge seems fairly unlikely

The mismatch in the red range has not been further investigated as part of this work.

5.3 Band Diagram of the Best Fit

Figure 17 shows the conduction band for the best-fit case at room temperature with and without illumination at 0 V and at 0.6 V forward bias. The peak barrier heights with respect to the conduction band in the bulk, deep in the device, are also given.

Operation in the dark:

The band offsets generate a barrier that acts like a secondary diode with the same polarity as the main diode. Thermal excitation of the carriers over the barrier is necessary for conduction. The peak-like shape suggests that the conduction could be enhanced by a tunneling process through the barrier under forward bias. This would lead to a constant “ kT ” product as it is observed in the IEC device. However, AMPS does not include tunneling processes in the computation of device characteristics.

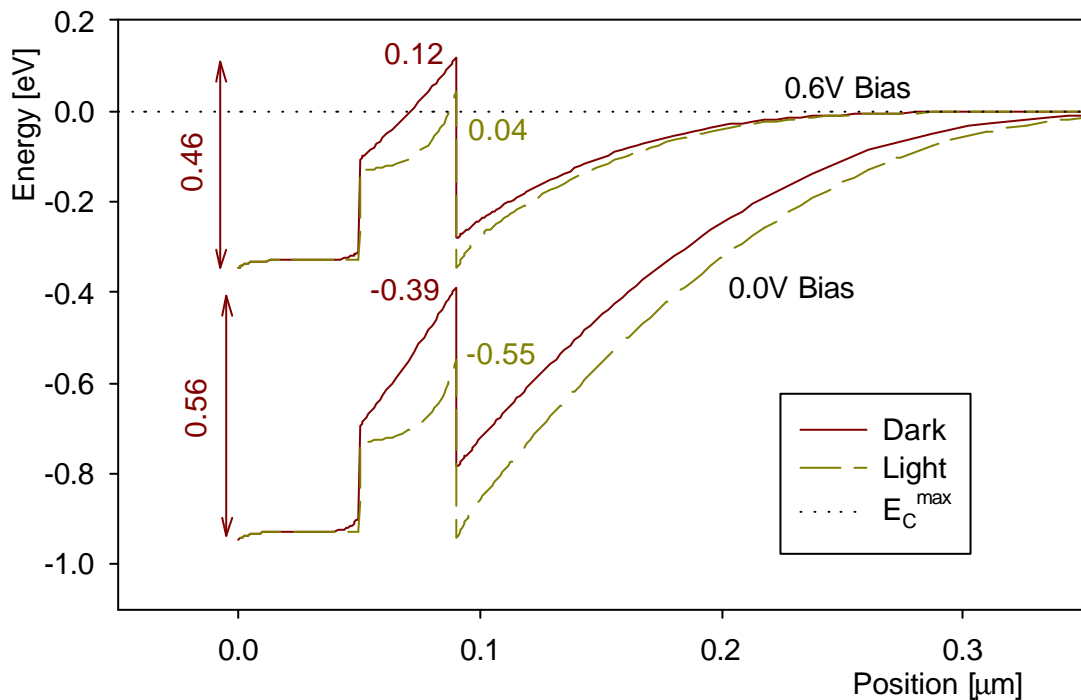


Figure 17: Best fit – conduction band diagram at $T = 298$ K

All of the deep acceptor states are ionized in the dark since there are no holes present that could be trapped into the deep states.

Under illumination:

The hole concentration in the n-type CdS layer is greatly increased by the photo-generation. The increased hole density leads to significant trapping of holes into the acceptor-like defect states, generating space charge that results in bending of the bands to a degree where the barrier does not greatly distort the J-V light characteristics. The bulk of the photons is absorbed in the CIGS close to the junction where the strong band bending creates a potential well for the electrons. The electrons accumulate in this well and overcome the barrier or recombine at the interface. If the barrier exceeds the bulk conduction band level considerably at voltages lower than V_{oc} , it would block the current flow and the light curves would be distorted as well (this was observed at low temperature in Section 5.4 with increased ΔE_{C2} , also see Section 5.6).

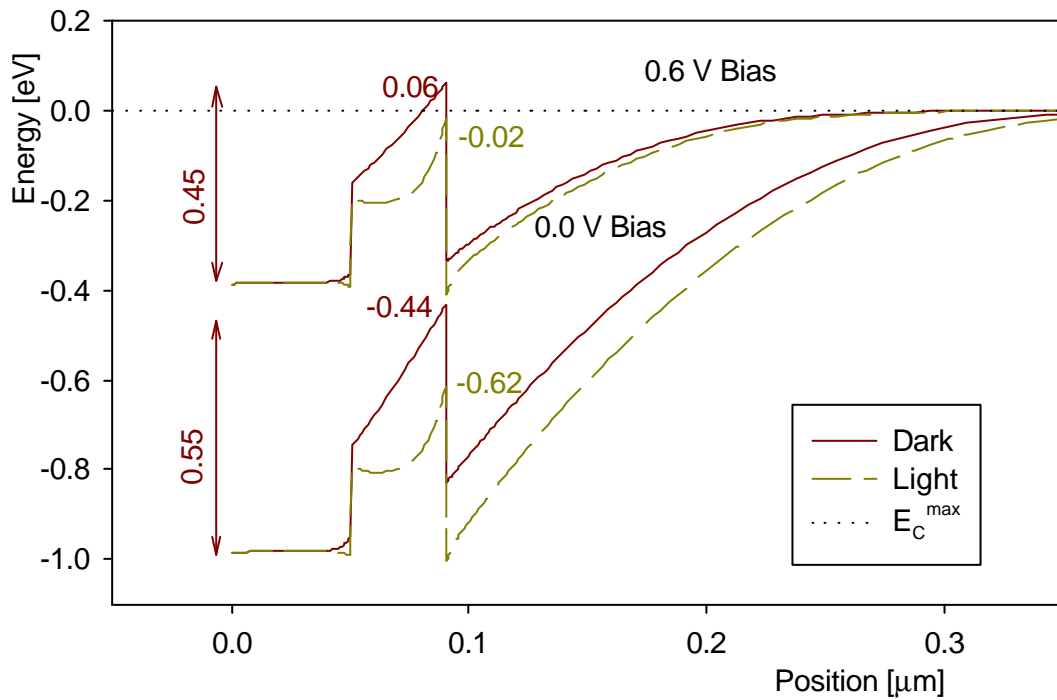


Figure 18: Best fit – conduction band diagram at $T = 238 \text{ K}$

Changing to lower temperatures, Figure 18, the band diagram does not change appreciably. The biggest difference is caused by the reduced thermal energy of the electrons (kT). At lower temperature, it becomes increasingly difficult for the electrons to overcome the barrier in forward bias; therefore, a shift to higher voltages is seen in the dark. Under illumination, the barrier is still negligible and the expected voltage progression ($\sim 1.9 \text{ mV/K}$) is observed.

5.4 Modeling: Variations on the Best Fit

In the next step, variations on the best fit were performed to investigate some of the voltage-temperature dependences in the light and dark. These variations are intended to cover parameters that are not accurately known, in order to support the validity of the chosen numbers. Plotted are, Figure 19-23, the results in terms of voltage shifts with respect to the best fit at $T = 298 \text{ K}$ (light and dark) and the progression of the voltage with temperature in mV/K . “Light” refers to changes in V_{oc} voltages and “Dark” voltages were measured at a positive current density of $J = |J_L|$.

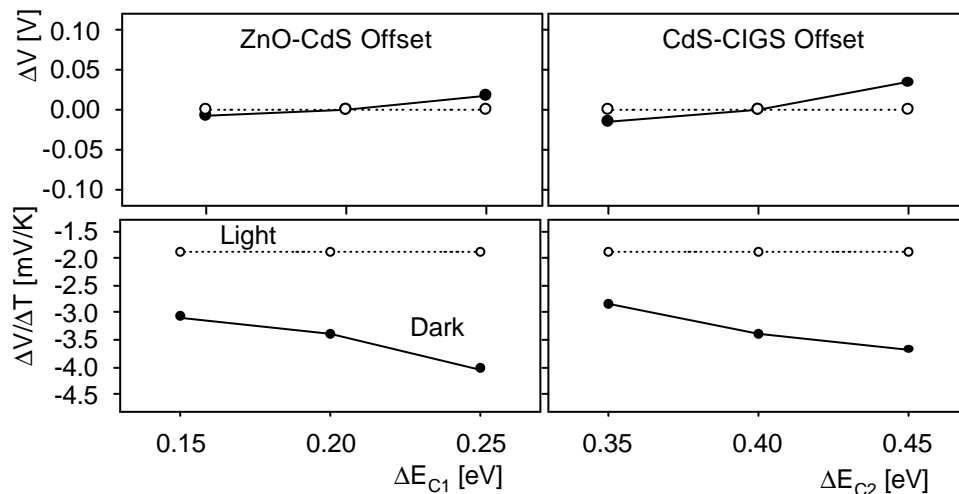


Figure 19: V-T - variation in band offsets (electron affinities)

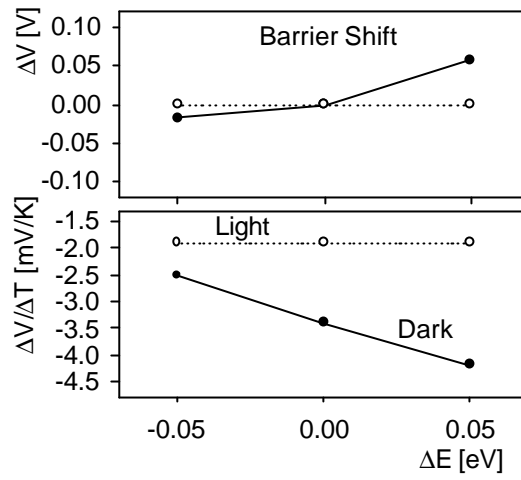


Figure 20: V-T - barrier shift (changing both offsets)

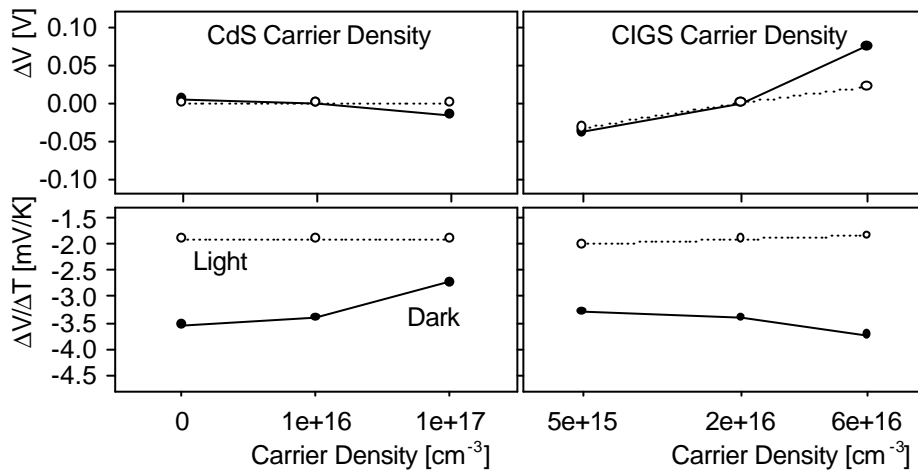


Figure 21: V-T - variations in carrier density in CdS and CIGS

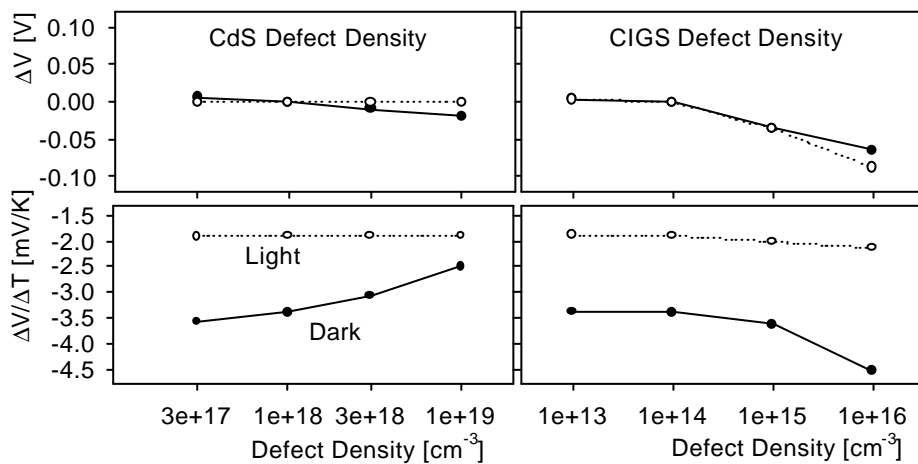


Figure 22: V-T - variations in defect density in CdS and CIGS

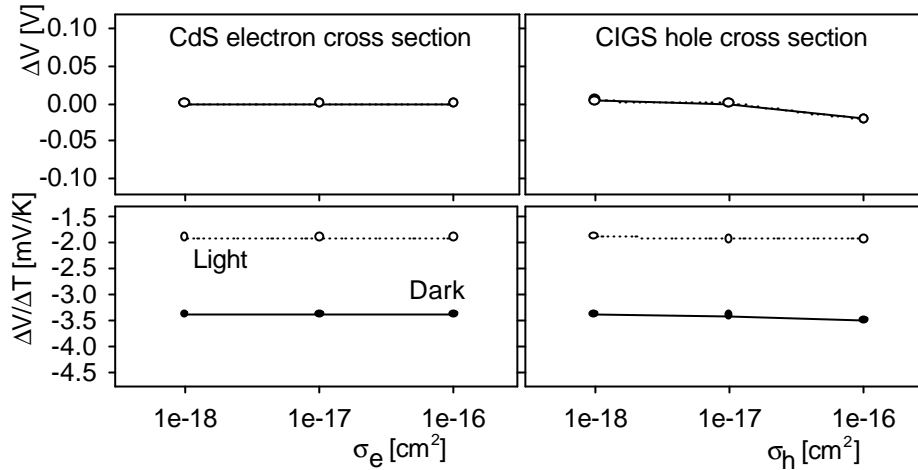


Figure 23: V-T - variations in capture cross-sections in CdS and CIGS

Band Offset Variations

Varying ΔE_{C1} or ΔE_{C2} (Figure 19 and 20) shifts the dark curve and changes the voltage progression. Higher offsets shift the curves to higher voltages and a smaller offsets to lower voltages. The light curves are unchanged by these variations. However, ΔE_{C2} changes also led to a loss in fill factor in the low temperature J-V curve. This indicates that increasing the offset beyond the chosen best fit value generates a barrier high enough that will reduce the light current as well as the dark current. Varying both offsets simultaneously, “adds” the effects of the ΔE_{C1} and ΔE_{C2} changes.

Carrier Densities

Increasing the effective carrier concentration in the CdS layer (Figure 21, left) stiffens the conduction band and leads to an overall lower barrier. Therefore, the voltage shifts down in the dark. The fact that an effective carrier concentration of zero ($N_D = N_{AG}$) does not induce strong changes, leads to the conclusion that the small fraction of deep acceptor levels that are neutral, given by $N_{AG}*(1-f_A)$, is comparable or greater than 10^{16} cm^{-3} . Higher carrier concentrations in the CIGS (Figure 21, right) lead to less band

bending in the CIGS and therefore a higher barrier. The overall voltage shift in the dark and light is described by the change in saturation current and is not related to the barrier.

Defect Densities

The effect of the CdS defect density (Figure 22, left) on the dark curves is similar to that of carrier density, since the small fraction of non-ionized defects adds to the carrier concentration and this contribution increases linearly with N_{AG} . In the light, a low CdS defect density generates a loss in fill factor at low temperature, similar to an increased ΔE_{C2} , since the barrier is not as strongly reduced. Lower CIGS defect densities (Figure 22, right) do not affect the voltage or its progression. Higher numbers, however, lead to largely increased recombination, apparently increasing the progression. Once recombination is strong enough to change V_{oc} (ΔV is non zero), the temperature progression of these curves is influenced by the temperature dependent cross-section.

Cross-Sections

The electron cross-section is not the limiting factor for the recombination process in the CdS. Therefore, results are nearly independent of σ_e . In the CIGS however, the hole cross-section strongly determines the recombination current. Larger cross-sections show similar results as higher defect densities.

5.5 Variation in Illumination Intensity

The previous discussion showed that the reduction of the barrier depends crucially on the photon absorption in the CdS layer. For further experimental confirmation, the effects of varying illumination intensities were investigated. Figure 24 shows the modeling results for light intensities of 100%, 10%, 1%, and in the dark. The calculated intensity was adjusted by increasing the reflectivity at the front surface:

$$R_i = 1 - \frac{F_i}{100\%} \cdot (1 - R_0) \quad (4.1)$$

where F_i are the desired fractions of AM1.5 intensity in percent, R_0 is the default (best fit) reflectivity (0.144) and R_i is the reflectivity needed. For better comparison, all curves are shifted on the J axis for a common current density at $V = 0$ V. The voltage at $J = 0$ mA/cm², labeled “ V_{oc} equivalent”, was extracted from this data.

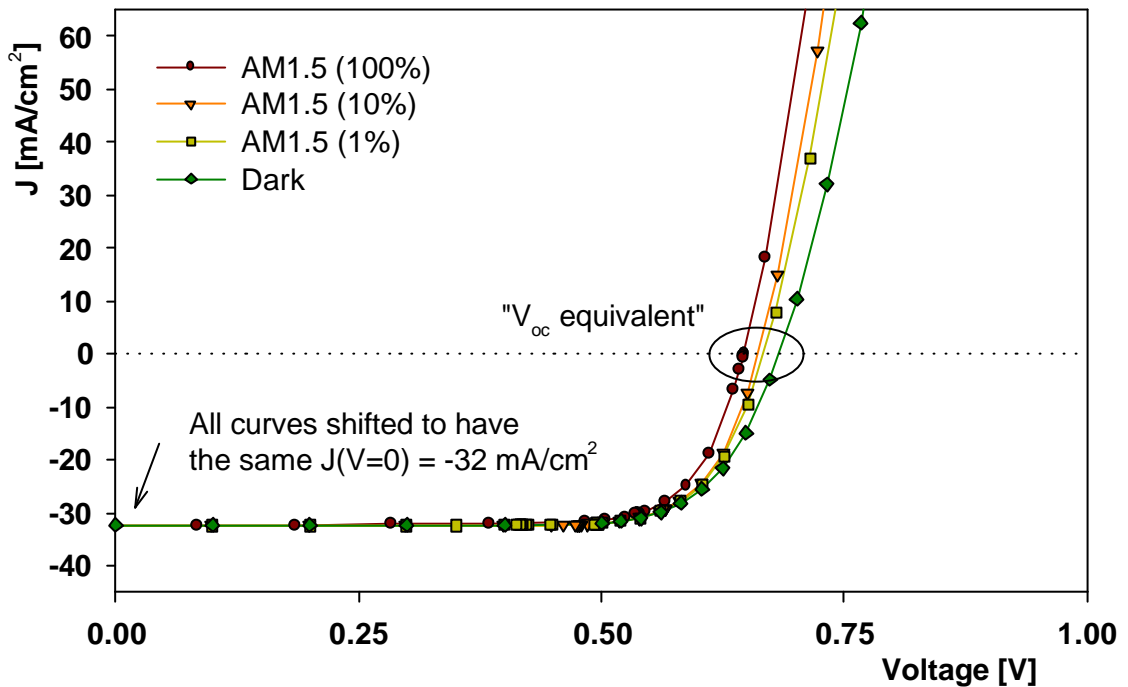


Figure 24: Modeled J-V for 100%, 10%, 1%, and 0% illumination

In comparison, experimental data is shown in Figure 25. The low level illuminations, 10% and 1%, show an irregular reduction in fill factor, which is not accounted for in the model. Conduction band diagrams for the modeling cases ($T = 298$ K) are shown in Figure 26. The barrier decreases continuously with increasing illumination. From this and similar plots the data shown in Figure 27 was extracted.

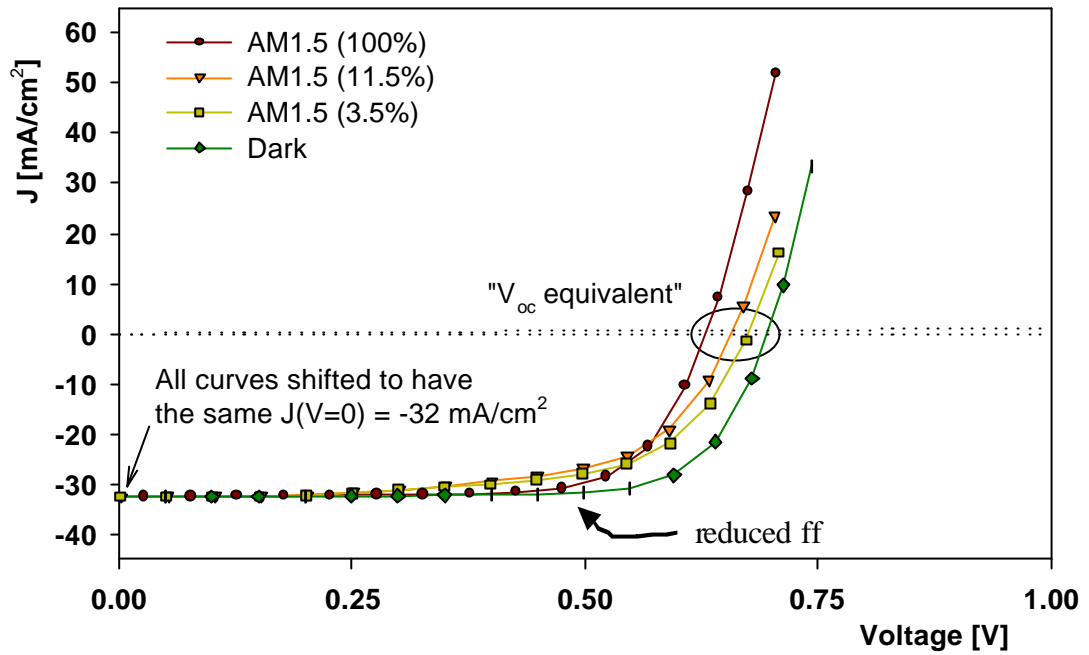


Figure 25: Experimental J-V for 100%, 11.5%, 3.5%, and 0% illumination

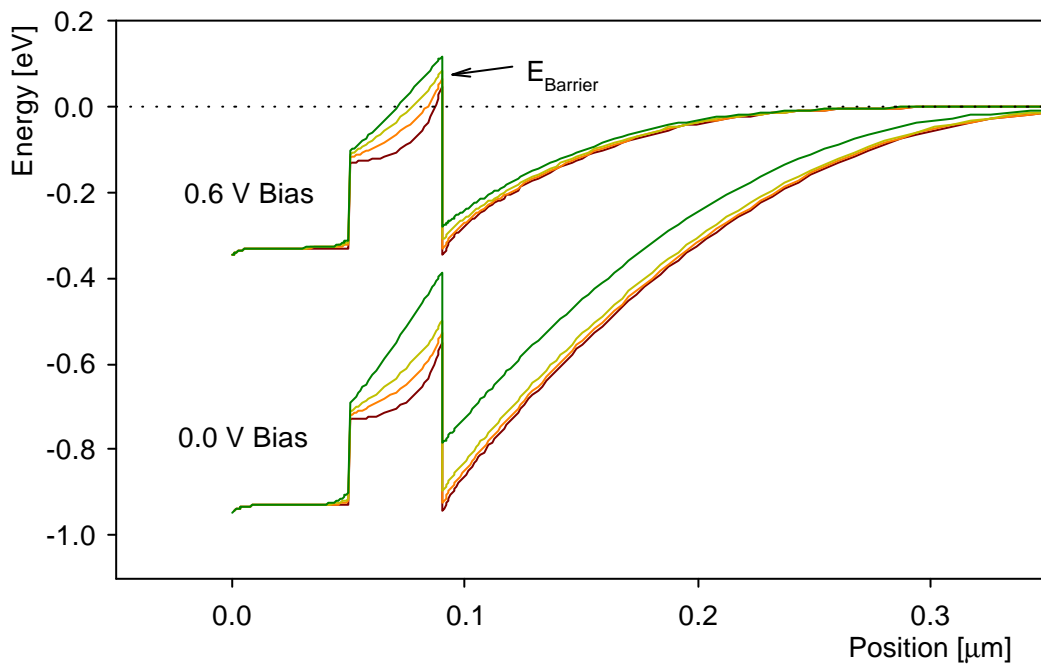


Figure 26: Band structure with varying illumination

Figure 26 and Figure 27 show that the illumination dependence of the barrier becomes weaker the further into forward bias the device is operated. This seems plausible, since in forward bias the CdS layer is less depleted, more free carriers are present, and

therefore the light-dark difference will become less significant. In comparison, Figure 27 also shows the progression of the “ V_{oc} equivalent”, deduced from the experimental and the modeling J-V data (Figure 24 and Figure 25). The experimental data follows the modeled barrier height progression closely, leading to the conclusion that the “ V_{oc} ” equivalent is mostly determined by the barrier height.

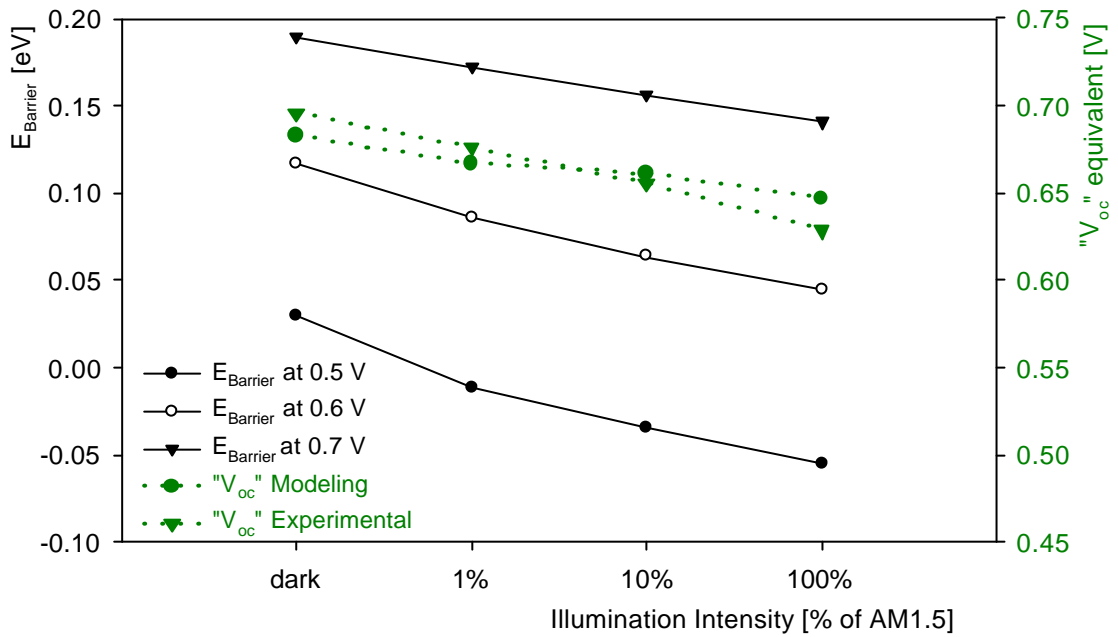


Figure 27: Barrier height and “ V_{oc} ” equivalent versus intensity

5.6 Single Wavelength Illumination and the “red kink”

Figure 28 shows J-V results for the best case under various single wavelength illuminations; the incoming flux was set to 2.4×10^{17} photons/cm²s, resulting in a maximum J_{sc} , which is approximately equal to the J_{sc} achieved under AM1.5 illumination. Below the CdS band gap ($\lambda \approx 515$ nm), the current is reduced due to the absorption and strong recombination (high defect density) in the CdS layer. Above the CdS band gap, the results are almost identical for all wavelengths and J-V curves become more rounded at

voltages close to V_{oc} . Photons with $\lambda \approx 515$ nm are not absorbed in the CdS and no holes will be generated that could be trapped into deep states and therefore, the barrier will not be reduced under light. The barrier being present under illumination blocks the current flow. Under red light illumination ($\lambda > 515$ nm) the following differences are observed: At voltages below V_{oc} , net current is negative and is reduced under red light (J-V shifted up), at voltages above V_{oc} , net current is positive and is also reduced under red light (J-V shifted down).

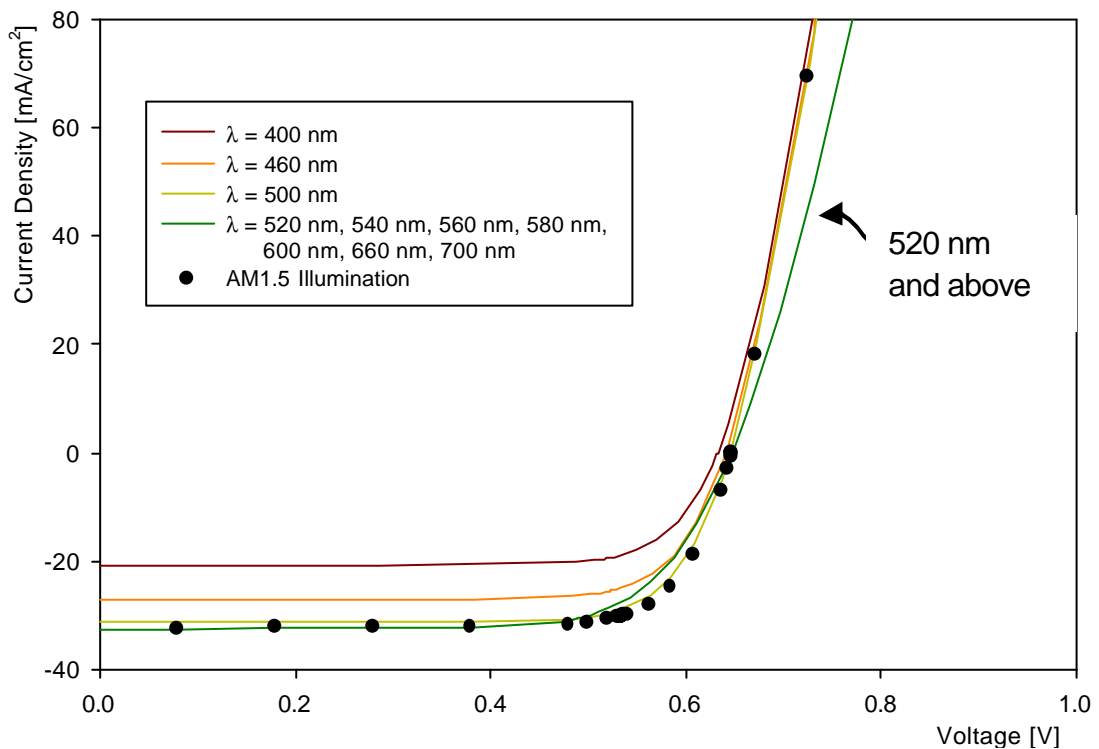


Figure 28: Calculated J-V with single wavelength illumination

Experimental J-V curves were measured using a red light filter (cutoff wavelength ≈ 610 nm). Unfortunately, the studied sample (described in Chapter 5.1) was no longer available. However, the measurements were done on a cell that was produced on the

same substrate as the earlier modeling target and it also showed unusual strong temperature progression. Resulting J-V curves (Figure 29) show qualitative agreement.

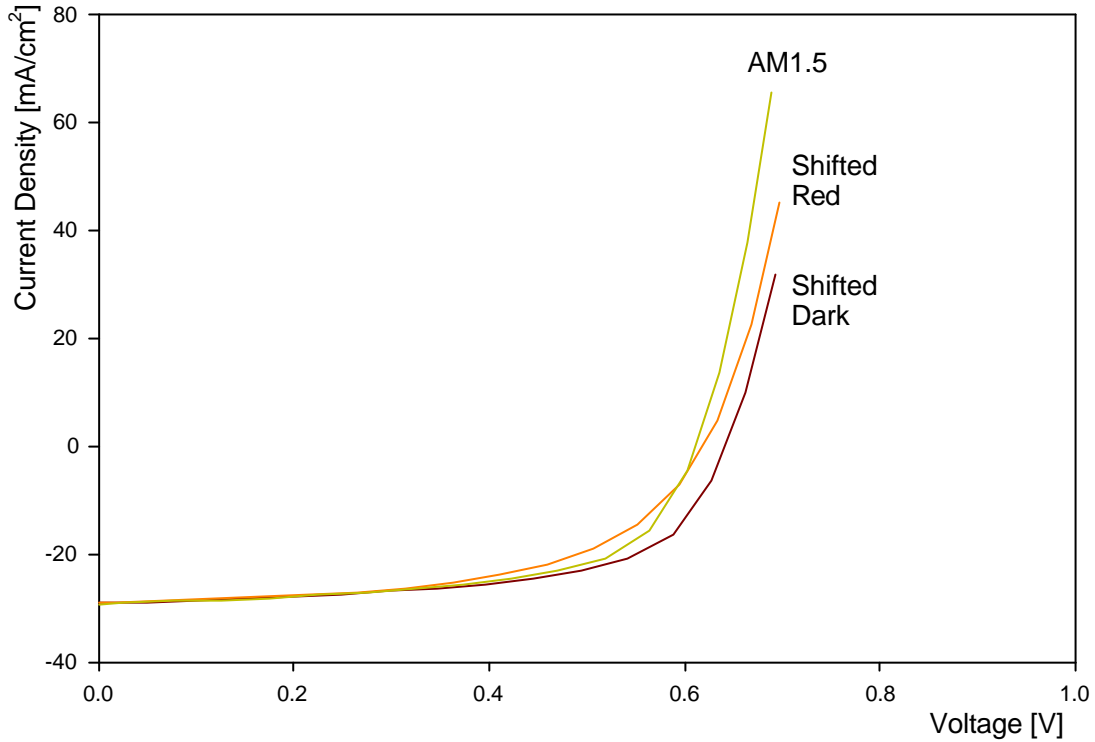


Figure 29: J-V at dark, red, and AM1.5 illumination (experimental)

The Red Kink

The general features of what is usually addressed as the “red kink” [14] are:

- a) reduced slope of current-voltage curve near V_{oc}
- b) strong cross-over of light and dark J-V
- c) effect a) and b) are observable only under red light or at least significantly reduced under white or blue light illumination

Figure 30 shows the best-fit case with varied band offsets $\Delta E_{C2} = 0.3$ eV, $\Delta E_{C2} = 0.4$ eV (best fit), $\Delta E_{C2} = 0.45$ eV, and $\Delta E_{C2} = 0.5$ eV under white light and single wavelength ($\lambda = 660$ nm) illumination.

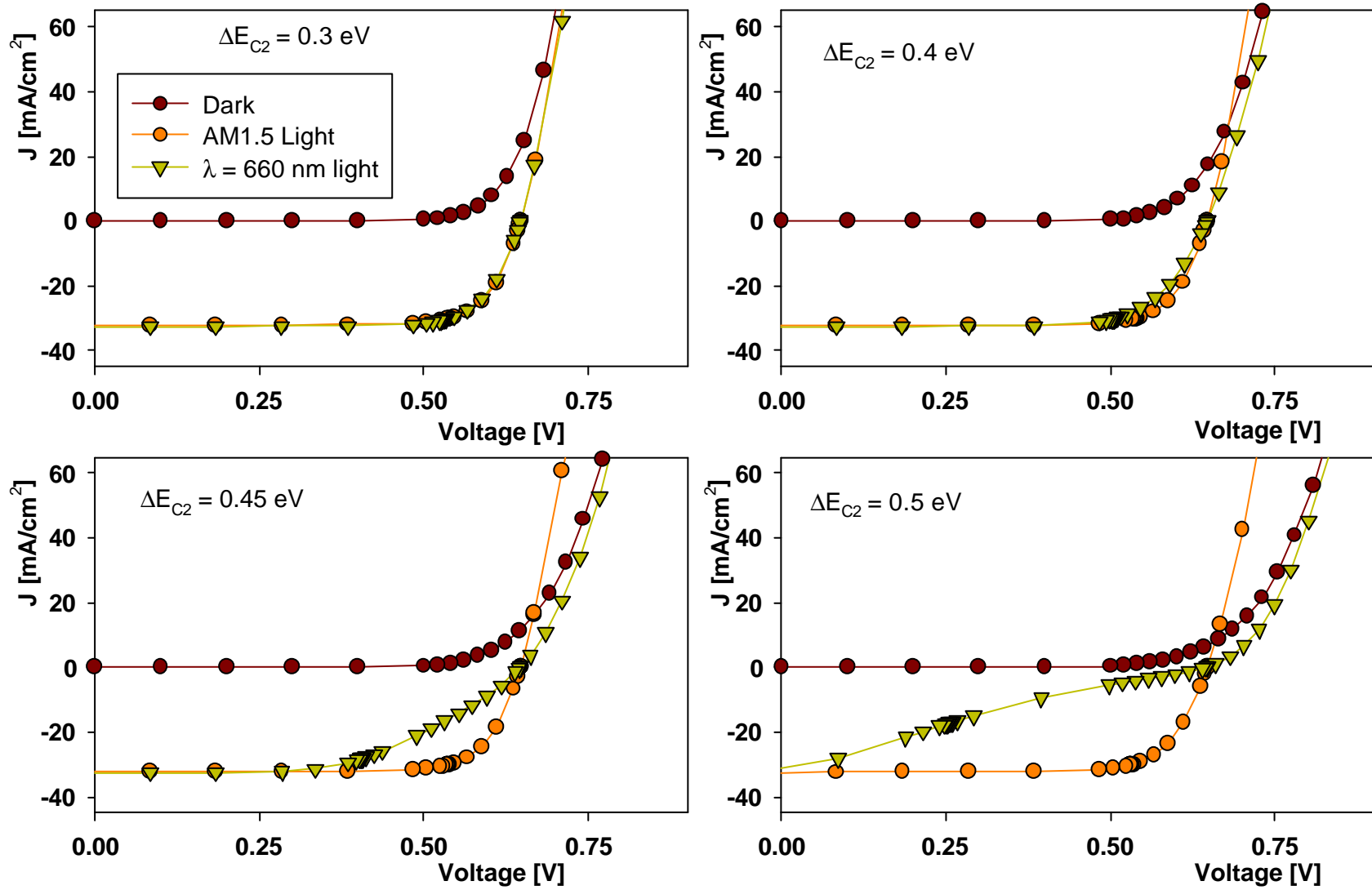


Figure 30: Red kink (modeling results)

For the small offset ($\Delta E_{C2} = 0.3$ eV), the superposition principle holds under either illumination. Offsets above 0.40 eV lead to the characteristic red kink behavior. Several publications, references [14]-[16], relate this observed effect to deep level acceptor states, which are present in the CdS or at the CdS-CIGS interface. While reference [14] and [16] see the necessary barrier being generated by the acceptor states themselves, reference [15] agrees with the currently proposed model of the barrier being generated by conduction band offsets and photogeneration in the CdS. Relaxation times for the deep acceptor-like trap states on the order of minutes to hours were reported in reference [15]. Dark measurements taken after exposure to white light (1 sun, 3 min.) yielded the same results at any time within 15 s – 10 min after the light was turned off, suggesting that no long time transient effects are present in the IEC sample used in this study. The results for the best-fit case, top row on the right, suggest that the device is in an intermediate situation where the barrier begins influencing the device performance under red light, but is not sufficiently large to cause the red kink.

5.7 Limitations of the Model

The approach that was taken here led to a model that was able to describe the basic principle of superposition failure as it occurs in CIGS devices. The model did not exactly match the experimentally measured J-V and QE curves and is therefore insufficient in some ways. This however, has to be expected considering the simplifications that were used defining the base case. The most likely shortcoming of the model used is the spatial distribution of defects in the CIGS absorber, especially near the CdS interface.

Chapter 6

Conclusions

This research has used the capabilities of computer simulation photodiode analysis to investigate CIGS solar cells. The selection of all input parameters for a reasonable baseline was presented. The parameters chosen generate light and dark current-voltage data that closely resembles that of a high efficient CIGS solar cell. Comprehensive studies on the influence of various device parameters were performed to confirm the validity of the model and improve the physical understanding of CIGS cells.

With small alterations to the baseline case, it was possible to successfully model a real device using a simple three-layer structure of ZnO/CdS/CIGS. An observed non-superposition effect in the experimental device could be explained by introducing band offsets of reasonable magnitude and a high density of acceptor-like defects in the CdS. The model was confirmed by comparing calculations and measurements with variations in illumination intensity and wavelength. Further investigation showed that a slight increase in the band offsets would lead to the occasionally observed red-kink effect.

Future work will concentrate on the application of the modeling technique to explain other failure mechanisms that are observed in experimental devices, for example induced by accelerated stress test. In addition, a more conclusive evaluation of experimental devices will be possible when modeling results are available for comparison.

References

- [1] United States Environmental Protection Agency, www link at <http://www.epa.gov/globalwarming/climate/index.html>, 08/14/2002
- [2] M.A. Contreras et al., *Progress in Photovoltaics* **7**, 311 (1999)
- [3] AMPS-1D Manual for Windows '95/NT, The Electronic Materials and Processing Research Laboratory at the Pennsylvania State University, University Park, PA 16802
- [4] M. A. Green, *Solar Cells*, Prentice-Hall, New Jersey, 1982
- [5] X.X. Liu, J.R. Sites, *J. Appl. Phys.* **75**, 577 (1994)
- [6] X.X. Liu, J.R. Sites, *AIP Conference Proceedings*, January 25, 1996, **353**, 444
- [7] A.L. Fahrenbruch, R.H. Bube, *Fundamentals of Solar Cells*, Academic Press, New York, 1983
- [8] S.H. Wei, A. Zunger, *Appl. Phys. Lett.* **63**, 2549, 1993
- [9] D. Schmid, M. Ruckh, H.W. Schock, *Solar Energy Materials and Solar Cells* 41/42 (1996), pp. 281-294
- [10] A.L. Fahrenbruch, *Modeling CdS/CdTe Solar Cells*, www link at <http://www.colostate.edu/orgs/pvlab/Pages/pdfDocs.htm>, 08/07/2002, pp. 5-6
- [11] S.M. Sze, *Physics of Semiconductor Devices*, 2nd Edition, John Wiley & Sons, New York, 1981
- [12] W. Shockley, W.T. Read, Jr., *Phys. Rev.* **87**, 835, 1952
- [13] R.C. Neville, *Solar Energy Conversion*, 2nd Edition, Elsevier, New York, 1995
- [14] J. Hou, S.J. Fonash, in *Proc. 25th Photovoltaic Specialists Conference (IEEE, Washington, 1996)* 961
- [15] I.L. Eisgruber, J.E. Granata, J.R. Sites, J. Hou, J. Kessler, *Solar Energy Materials and Solar Cells* 53 (1998), pp. 367-377
- [16] M. Topiè, F. Smole, J. Furlan, M.A. Contreras, 14th European Photovoltaic Conference (Barcelona, 1997) 2139